Lattice structure design optimization under localized linear buckling constraints

Ming Li[a,*], Yongcun Song[b], Xingtong Yang[a], Kai Zhang[c]

[a] *State Key Laboratory of CAD&CG, Zhejiang University, Hangzhou, China*
[b] *Chair for Dynamics, Control and Numerics, Alexander von Humboldt-Professorship, Department of Data Science, Friedrich-Alexander-Universität Erlangen-Nürnberg, 91058 Erlangen, Germany.*
[c] *Department of Mathematics, Jilin University, Changchun, China*

Abstract

An optimization method for the design of multi-lattice structures satisfying local buckling constraints is proposed in this study. In order to resolve the highly nonlinear large-scale optimization problem, a consecutive numerical approach is devised: macro-field optimization and microstructure embedding. The macro-field optimization finds an optimal elasticity tensor distribution among all feasible elastic continua based on a concept of free material optimization (FMO), which largely extends the design space compared with density-based topology optimization. After this, by an inverse design approach that approximates the elasticity tensor under local buckling constraint, an appropriate lattice structure is able to be embedded within each macro-element, where the local stress tensors are considered in particular to produce more reasonable microstructures. During the process, a machine learning approach is also devised to significantly reduce the number of material/lattice types and thus the overall computational costs. Ultimately, a lattice structure under requirements of overall stiffness and local buckling resistance is produced, as demonstrated via numerical examples.

Keywords: Local buckling mode; lattice structure; free material optimization; inverse homogenization; topology optimization.

1. Introduction

Lattice structures have fascinating properties of lightweight and multi-functions such as shock resistance [1], energy absorbability [2], damping enhancement [3], heat manipulation [4], and defect tolerance [5, 6]. With the fast development of additive manufacturing, reliable and efficient fabricating such complicated lattice structures has become practically possible, and boosted various related research developments and practical applications [7, 8, 9]. These prominent properties make them an ideal candidate in widespread industrial applications including aerospace, automotive, and biomedical field [10, 11]. Recent developments and applications of the lattice structures are further referred to the reviews from Dong et al. [12] and Tamburrino et al. [13].

Automatic design of a complex lattice structure to meet critical mechanical requirements on the other hand becomes a dominating task. Topology optimization is becoming a powerful automatic

*Corresponding author: liming@cad.zju.edu.cn

design tool that computes the optimal material distribution to meet certain design target and constraints, and various excellent approaches have been proposed over the past decades [14, 15, 16, 17, 18]. The approaches for lattice structure design mainly depend on a homogenization-based framework, where topologies of the micro-structures and/or their distributions are optimized for an overall structural performance optimization, usually stiffest structure [19, 20, 21, 22], or for the identification of periodic microstructure shapes approaching the theoretical limit on elastic properties [23, 24, 25, 26], or metamaterials for heat manipulation [4].

However, an extremely stiff lattice cell or structure may still fail as the appearance of slender lattice bars is very vulnerable to highly localized buckling when being imposed by compressive loading. Actually, it has been reported that the strength design achieved in industrials is still far from the theoretical strength limit it can achieve [27]. Noticing that the buckling design often has a counter-acting character to compliance or stress designs, it must be carefully incorporated into the optimization of such complex structures.

Topology optimization of a lattice structure under buckling constraint is however a more challenging topic than solely considering stiffness optimization. The challenges mainly come from its much more complex computational efforts, and the poor convergence. The computational costs are due to its eigenvalue analysis for the complex structures of extremely high DOFs. The convergence issue comes from the highly nonlinear optimization both in the coupled macro- and microstructures and the typical challenges encountered in the eigenvalue optimization problem, including eigenvalues with multiplicity or spurious local buckling modes [28, 29].

Previous work on topology optimization under buckling constraint mainly focuses on macroscale optimization or periodic microstructure optimization. Topology optimization of continuum structures with a global buckling criterion has been long considered by Neves et al [28], and later geometrically non-linear response was included in [30, 31, 32].

The problem of designing a microstructure under buckling constraint was initially considered by Bendsoe and Triantafyllidis [33] as a size optimization problem for a rectangular orthogrid. Subsequently, a topology optimization formulation for microstructure design under buckling constraint was formulated by Neves et al. [28], which treated localized instability modes under an assumption of cell-periodic wavelengths. The study was then extended to further cover non-local buckling modes using the Bloch-wave technique in [29, 34]. Later on, the researchers have conducted a series of excellent studies on optimizing microstructures under buckling constraints [35, 36, 37, 38]. In particular, Thomsen et al. [35] optimized periodic microstructures with respect to multiscale buckling conditions under representative stress situations, laying the foundations for future multiscale structural and material design. Wang and Sigmund [36] investigated the stiffness and buckling strength of finite structure consisting of periodic microstructures, and optimized the microstructures with enhanced buckling strength. Here, the effects under two benchmark loadings were considered: uniaxial compression loading and shear loading. Research efforts have also been devoted to designing 2D or 3D microstructures with tunable stiffness and buckling properties [39, 37]. Very recently, Christensen et al proposed a multiscale topology optimization approach that takes into account both the global and local bucking constraints [38]. In most of these previous studies, the applied techniques are mainly based on the homogenization theory, linear buckling analysis, and Bloch-Floquet theory, which worked together to reduce the computational costs and to account for short and long wavelength buckling.

In spite of the achievements from these previous studies, designing a lattice structure to maximally resist the local buckling while simultaneously maintaining the global structure stiffness seems

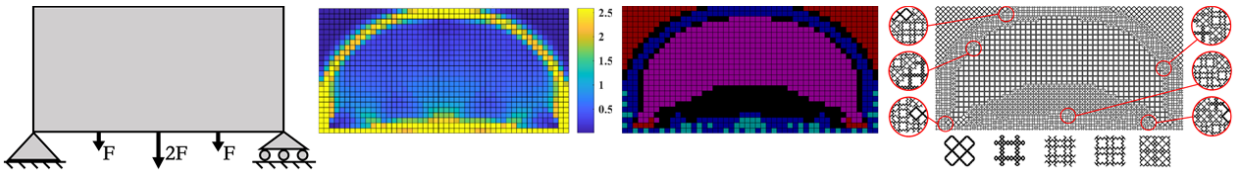

Figure 1: Overview of the proposed method (from left to right): problem definition, finding an optimal elasticity tensor distribution, clustering to obtain discrete solutions, inverse microstructure design under buckling constraint to produce the final lattice structure design.

to be rarely addressed as far as we know, which is to be explored in this study. The optimization framework has to address the critical issues as how to resist local buckling without much losing the global structural stiffness. Besides the above mentioned critical issues, it has to further take into account other important challenges on generating a geometrically valid lattice structures, reducing the types of lattice cells, and effectively decoupling between the macro-structure and the micro-lattices to reduce the overall computational complexities.

This is to be achieved in this study via a two-step process by first conducting free material optimization (FMO) by computing optimal material distribution within a coarse mesh, then embedding microstructures under buckling constraints. During the process, a machine learning approach is also devised to significantly reduce the number of material/lattice types, and consequently the associated lattice cells to be optimized and the overall computational costs. Ultimately, a lattice structure with overall optimized stiffness and local buckling resistance is produced that enhances the structural mechanical properties as demonstrated via numerical examples.

The remainder of the study is arranged as follows. The method is first overviewed in Section 2. The numerical details on the macroscale design and microscale design are respectively presented in Sections 3, 4, and 5. After demonstrating the method's performance on 2D examples in Section 6, the study is concluded in Section 7.

2. Overview

Previous researches on topology optimization of continuum structures have produced many excellent results on improving structural stiffness. These approaches mainly take structural stiffness as the performance evaluation criterion, and seldom address challenges such as stress concentration or structural buckling. The obtained designs usually lead to structural instability or fractures in practical engineering investigations, resulting in energy loss. Therefore, it has been widely acknowledged the need to further incorporate both stress and buckling requirements, rather than just stiffness, into the lattice design in order to improve the structural overall performance [40]. Our study mainly focuses on the stiffness optimization problem under the buckling constraints.

In order to obtain a stable optimized structure, additional consideration of buckling constraints is required. Without considering the computer arithmetic limitations, if a high-resolution underlying density mesh is used as much as possible, it often tends to generate fine rod-like structures that are usually subject to buckling failure. Consider for example the excellent work of Aage et al [41] that studied a full-scale wing-design problem in giga-voxel-resolution. The generated structure contains a large number of intricate details like curved beams or trusses, which usually result in undesirable buckling performance. It is noteworthy that these detailed complex structures often

differ significantly in size and scale from the overall structures. Therefore, it is very desirable to impose the buckling constraints on the local microstructures.

Regarding the structural buckling in a biscale topology optimization of continuum structures, properly resolving the optimization problem and reducing the overwhelming computational burden pose serious challenges. The causes of the challenges come from such issues as highly coupled macro- and micro- formulations, non-robust sensitivity analysis from mode switching and multimode, and the costly de-homogenization in producing different microstructures.

These issues are to be resolved in several aspects. Firstly, the optimal elastic distribution within the overall structure is derived via an FMO approach which directs the subsequent work on lattice cell embedding. The separate FMO and microstructure embedding allows us to work on two relatively simper optimization problems. The FMO, in comparison with a density-based optimization, increases the design space to produce a possible better structure. In addition, in order to reduce the number of lattice cells to be de-homogenized, which is generally the most computational costly work, the resulted free material are clustered into a small group of different elasticity tensors. The clustering process also increases the overall structural periodicity so that a homogenization-based analysis and optimization could be more reasonably applied.

Secondly, the microscopic model is composed of smoothly blended lattice bars and the buckling constraints are imposed on their design optimization. The strategy ensures to produce a geometrically valid structure and much reduces the number of design variables. It does not require additional expensive reconstruction efforts in producing a geometrically valid structure.

Thirdly, the buckling constraints are aggregated into a single one using the K-S aggregation function [42] and incorporated into the objective function. In fact, the large number of buckling constraints may deteriorate the optimization convergence in two aspects: mode switching and multimode can appear during the optimization process, and the repeated eigenvalues associated with multimode are even non-differentiable. The K-S based strategy helps to derive a reliable sensitivity analysis.

Furthermore, the buckling response of a microstructure is analyzed under a given stress condition derived from the macroscopic analysis. We specifically select the stress condition on each type of clustered lattice cells based on the results of the finite element analysis on the macroscopic real-world solution. This way, the optimized structure is more compatible with the macroscopic target as compared with conventional approaches that generally set a general stress for representative cell. Owning to the clustering process, the stress is selected as the maximal one amongst the elements within each cell type.

In this step, we focus on the overall FMO-based framework to design lattice structures under linear buckling constraint. The local buckling mode taken here is treated under an assumption of cell-periodic wavelengths following the formulation from Neves et al. [28]. In case that the lowest bucking mode spans a group of adjacent macro-cells, the Bloch-Floquet boundary condition has to be imposed to capture both the short and long wavelength buckling. More details are referred to the excellent work from Neves [29, 34], Wang and Sigmund [36, 37], and Christensen et al [38].

Based on the above considerations, this study proposes a multiscale optimization approach under local buckling constraints; see Fig. 1 for an illustration. We first compute an optimal distribution of the material elasticity tensor associated to each macro-element based on an approach of free material optimization. The free material properties are further clustered into a small group of different elasticity tensors based on a machine learning technique to accelerate the downstream tasks. The FMO-based approach broadens the design space as compared with conventional density-

based approaches. After this, the lattice structure is to be found for each macro-element by an inverse design process that approximates the elasticity tensor under the buckling constraint. Here, the location stress is also included for a further improvement of performance optimization based on an observation that the buckling mode does not only depend on its shape of microstructures but also on its external loadings. It ultimately produces a multi-lattice structure with improved local buckling modes.

3. Optimal material tensor field generation in macroscale

This paper focuses on the classical problem of maximizing the stiffness of a structure under certain boundary and stability (buckling) conditions defined in a multiscale sense. This section first explains the modeling and computational approach of the macroscale problem to find an optimal elasticity tensor distribution among all feasible elastic continua. After this, a novel material clustering approach is applied to reduce the material space while simultaneously maintaining high compliance fidelity of the generated structure.

3.1. Optimal material distribution via FMO

The problem of FMO takes the material elasticity tensor in each domain point as design variables, and finds their optimal distribution within the design domain. Without loss of generality, we consider in the rest of the study a 2D macro-design domain $\Omega = \{\omega_i, i = 1, \dots, M\} \subset \mathbb{R}^2$ composed of discrete disjoint square elements ω of the same size. For each ω, let $\boldsymbol{\sigma}_\omega$ and $\boldsymbol{\varepsilon}_\omega$ be the second-tensor stress and strain vectors using the conventional Kelvins notation

$$\boldsymbol{\varepsilon}_\omega = (\boldsymbol{\varepsilon}_{11}, \boldsymbol{\varepsilon}_{22}, \sqrt{2}\boldsymbol{\varepsilon}_{12})^T, \boldsymbol{\sigma}_\omega = (\boldsymbol{\sigma}_{11}, \boldsymbol{\sigma}_{22}, \sqrt{2}\boldsymbol{\sigma}_{12})^T, \tag{1}$$

where

$$\boldsymbol{\varepsilon}_\omega = \frac{1}{2}\left(\nabla \mathbf{u}_\omega + \nabla \mathbf{u}_\omega^T\right),$$

$\mathbf{u}_\omega \in \mathbb{R}^8$ is the associated displacement vector and ∇ is the gradient operator.

It follows from the Hooke's law ([43]), the stress is a linear function of the strain in the following form

$$\boldsymbol{\sigma}_\omega = \mathbf{D}_\omega \boldsymbol{\varepsilon}_\omega, \tag{2}$$

where the elasticity tensor $\mathbf{D}_\omega$ is a symmetric positive 3×3 matrix

$$\mathbf{D}_\omega = \begin{bmatrix} \mathbf{D}_{1111} & \mathbf{D}_{1122} & \sqrt{2}\mathbf{D}_{1112} \\ \mathbf{D}_{1122} & \mathbf{D}_{2222} & \sqrt{2}\mathbf{D}_{2212} \\ \sqrt{2}\mathbf{D}_{1112} & \sqrt{2}\mathbf{D}_{2212} & 2\mathbf{D}_{1212} \end{bmatrix}. \tag{3}$$

The elasticity tensor matrix can also be of orthogonal material subject to the following conditions

$$\mathbf{D}_\omega = \begin{bmatrix} \frac{E_x}{1-\nu_{xy}\nu_{yx}} & \frac{\nu_{yx}E_x}{1-\nu_{xy}\nu_{yx}} & 0 \\ \frac{\nu_{yx}E_y}{1-\nu_{xy}\nu_{yx}} & \frac{E_y}{1-\nu_{xy}\nu_{yx}} & 0 \\ 0 & 0 & G_{xy} \end{bmatrix} \tag{4}$$

and $\nu_{xy}E_y = \nu_{yx}E_x$. Here, E_x, E_y stand for Young's modulus, ν_{yx}, ν_{xy} are Poisson's ratios and G_{xy} is shear modulus. It can also be of isotropic material governed by its Young's modulus and

Poisson's ratio. Our proposed framework is able to handle different cases, and we mainly focus on the case of general elasticity tensor for the ease of explanation.

The free material optimization problem aims to find the optimal material property $\mathbf{D}_\omega$ associated with each ω such that the resulted structure is stiffest, that is, find $\mathbf{D} = (\mathbf{D}_1, \ldots, \mathbf{D}_M)$ so that the compliance of the resulted structure $(\Omega, \mathbf{D})$ is minimized, that is,

$$\min_{\mathbf{D}_\omega \in \mathbb{S}^{\mathbb{N}}_+} C(\mathbf{D}, \mathbf{u}) = \mathbf{f}^T \mathbf{u}, \quad s.t. \tag{5}$$

$$\begin{cases} \mathbf{K}(\mathbf{D})\mathbf{u} = \mathbf{f},\ \mathbf{u} \in \mathcal{U}, & \text{equilibrium equation} \\ \sum_{\omega=1}^{M} \mathrm{Tr}(\mathbf{D}_\omega) \le m_f T_0, & \text{global trace constraint} \\ \underline{T} \le \mathrm{Tr}(\mathbf{D}_\omega) \le \overline{T}, \ \ \omega = 1, \ldots, M, & \text{element trace constraints} \\ \mathbf{D}_\omega - \delta \mathbf{I} \in \mathbb{S}^{\mathbb{N}}_+, \ \ \omega = 1, \ldots, M, & \text{manufacturability constraint.} \end{cases}$$

In the above equation, the objective function $C(\mathbf{D}, \mathbf{u})$ is the structure's compliance calculated by

$$C(\mathbf{D}, \mathbf{u}) = \mathbf{u}^T \mathbf{K}(\mathbf{D})\mathbf{u} = \sum_{\omega=1}^{M} \mathbf{u}_\omega^T \mathbf{K}_\omega(\mathbf{D})\mathbf{u}_\omega, \tag{6}$$

$\mathbf{u}$ is the macroscopic displacement field, $\mathcal{U} \subset \mathbb{R}^d$ is the admissible displacement space, where certain Dirichlet boundary conditions are prescribed, $\mathbf{f}$ is the exerted nodal force vector ignoring the structure weight for simplicity, and $\mathbf{K}(\mathbf{D})$ is the global stiffness matrix calculated by

$$\mathbf{K}(\mathbf{D}) = \sum_{\omega=1}^{M} \mathbf{K}_\omega(\mathbf{D}), \ \ \mathbf{K}_\omega(\mathbf{D}) = \sum_{k=1}^{n_G} \mathbf{B}^T \mathbf{D}_\omega \mathbf{B},$$

where $\mathbf{B}$ is the strain-displacement matrix and n_G is the number of Gaussian integration points. Note that $\mathbf{K}$ and $\mathbf{K}_\omega$ are all symmetric positive semidefinite.

Constraints on the material usage is prescribed by the traces of each elasticity tensor $\mathbf{D}_\omega$ and their sum. Specifically, $\mathrm{Tr}(\mathbf{D}_\omega)$, the trace of $\mathbf{D}_\omega$, denotes the elemental material cost, which is bounded by $\underline{T}$ and $\overline{T}$, and $m_f T_0$ constrains the overall amount of materials distributed within the structure for a fraction parameter m_f with respect to trace T_0 of a full solid material.

The last constraints above impose additional manufacturability constraints to bound the minimal eigenvalues of elasticity tensors away from zero, in case that any directional stiffness is too close to zero [44, 45] for a small quantity δ greater than zero. Here, $\mathbb{S}^{\mathbb{N}}_+$ is the cone of symmetric positive semidefinite matrices in the space $\mathbb{S}^{\mathbb{N}}$ of symmetric $N \times N$ matrices for $N = 3$ in 2D, $N = 6$ in 3D. The value of the desired δ varies with different design problems, and can be computed using the method described in [46]. Note here there is a notable fact that without the last constraint, the original problem (7) will generate some extreme elasticity tensors which usually make the subsequent microstructure design difficult or even impossible.

Lemma 1. *([44, 45]) The FMO problem* (5) *includes nonlinear and nonconvex vector constraints. Using the Schur complement theorem, this nonconvex semi-definite programming (SDP) problem can be written as follows*

$$\min_{\mathbf{D}_\omega \in \mathbb{S}^{\mathbb{N}}_+, \gamma > 0} \gamma, \quad s.t. \tag{7}$$

$$\begin{cases} \begin{pmatrix} \gamma & \mathbf{f}^T \\ \mathbf{f} & \mathbf{K}(\mathbf{D}) \end{pmatrix} \geq 0, \\ \sum_{\omega=1}^{M} \mathrm{Tr}(\mathbf{D}_\omega) \leq m_f T_0, \\ \underline{T} \leq \mathrm{Tr}(\mathbf{D}_\omega) \leq \overline{T}, \quad \omega = 1, \ldots, M, \\ \mathbf{D}_\omega - \delta \mathbf{I} \in \mathbb{S}_+^{\mathbb{N}}, \quad \omega = 1, \ldots, M. \end{cases}$$

If without the last constraint, the above problem becomes a linear SDP problem, which has a converged global optimum. Even though the solution to problem (7) becomes sub-optimal after adding the last constraint, the downstream task of microstructure embedding is still much facilitated [47]. The solution to the above FMO problem can be computed efficiently via a primal-dual interior point method. For isotropic material optimization problems, the methods described in our previous work [48] can be consulted.

3.2. Material space reduction via hierarchical clustering

The derived material distribution of elasticity tensors $\{\mathbf{D}_\omega,\ \omega = 1, \ldots, M\}$ from the FMO is highly heterogeneous within the design domain, in the sense they are almost different from each other. This poses serious challenges to the practical applications of the optimization results, such as the huge computational costs to design respectively the embedded microstructures, the difficulties of their reliable manufacturing and the costs of testing their physical properties for such a huge number of varieties.

The issues are to be resolved by an unsupervised machine learning approach that clusters the material tensors into a small number of clusters. Different clustering algorithms have been developed in the past, such as K-means, mean-shift, Gaussian mixture model etc. For our specific task of clustering elasticity tensors, it is hoped: 1. Different numbers of clusters can be easily derived from different design purposes. 2. The larger number of clusters, the better lattice structure is to be achieved.

An agglomerative hierarchy clustering algorithm is carefully selected and developed for the purpose. It groups data on various scales by creating a clustering tree. The tree is not a group of individual clusters, but a multi-level hierarchy, in which clusters at one level are connected together as clusters at the next level. The overall algorithm of the hierarchical clustering works as follows:

1. Initialize each cluster as the elasticity tensor $\{\mathbf{D}_\omega,\ \omega = 1, \ldots, M\}$ computed from Eq. (7).
2. According to the similarity measure explained below, find the nearest pair of clusters and combine them into a single cluster, resulting in $M - 1$ clusters.
3. Based on the agglomerative clustering linkage algorithm to measure the distance between different cluster, and cluster the nearest into a single cluster.
4. According to user's specification or classic measure such as Silhouette score, output the optimal number of clusters and their associated tensors, that is $\{\mathbf{D}_k,\ k = 1, \ldots, K\}$, for a much smaller number K of clusters, where each $\mathbf{D}_\omega$ belongs to a certain group of $\mathbf{D}_k$.
5. Decide the corresponding cluster center by performing again the following FMO process, defined below,

$$\min_{\mathbf{D}_\omega \in \mathbb{S}_+^{\mathbb{N}}, \gamma > 0} \gamma, \quad s.t. \tag{8}$$

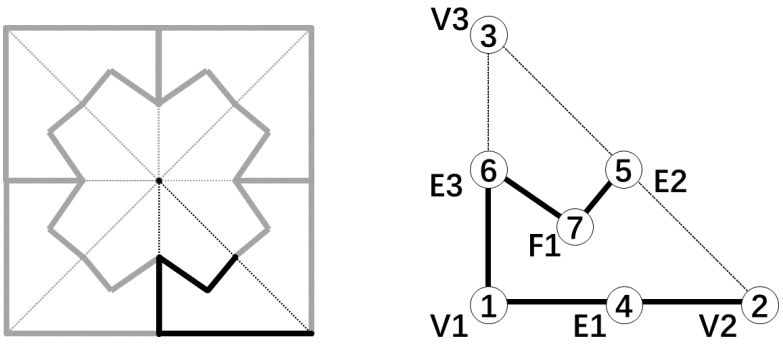

Figure 2: A schematic diagram of a complete microstructure model and its one-eighth.

$$\begin{cases} \begin{pmatrix} \gamma & \mathbf{F}^T \\ \mathbf{F} & \mathbf{K}(\mathbf{D}) \end{pmatrix} \geq 0, \\ \sum_{k=1}^{K} \sum_{\omega \in \Xi_k} \mathrm{Tr}(\mathbf{D}_\omega) \leq m_f T_0, \\ \underline{T} \leq \mathrm{Tr}(\mathbf{D}_k) \leq \overline{T},\ k = 1, \ldots, K, \\ \mathbf{D}_k - \delta \mathbf{I} \geq 0,\ k = 1, \ldots, K, \end{cases}$$

where the integer K is the prescribed number of cluster groups. Note the trace sum of $\mathbf{D}_\omega$ is still computed on all elements in the design domain.

In step 2, various distance measures can be defined such as Euclidean distance, Minkowski distance, Manhattan distance or Cosine similarity. The classical Euclidean distance for anisotropic elasticity tensors is finally selected after tests. For isotropic material, we follow the approach in [49] to measure their similarity in an intrinsic material property space, which demonstrates nice performance as verified experimentally. In step 3, measures via single linkage, complete linkage, or average linkage exist, and the complete linkage is chosen. More details on hierarchical clustering are referred to [50].

4. Lattice structure modeling and analysis in microscale

According to the above operations, we can obtain a set of discrete elasticity tensors and their distribution within the design domain. Further mechanical analysis also gives the stress distribution. Accordingly, each element is then to be embedded with a microstructure via an inverse homogenization theory under pre-specified buckling constraints in combination with the element stress. This section first elaborates the modeling and buckling analysis of these micro-lattice structures.

4.1. Lattice structure modeling in implicit form

Basically, a lattice cell can be modeled in a parametric form, an implicit form, or a discrete mesh form. The implicit form has its merits in ease of freeform modeling, blending generation, boolean operations etc, and is taken here for lattice structure modeling. The lattice cell is defined by a set of bars of connecting nodes in a square element. It is prescribed within a 1/8 of a square element; a mirror symmetry gives the overall cell; see Fig. 2. The following notations are used:

Ω: a given solid model;

$\mathcal{M}$: a quadrilateral mesh of Ω;

ω: a macro-element of Ω, each consisting of a set of fine elements ω_ω;
$\mathbf{v}_1^{(i)}, \mathbf{v}_2^{(i)}$: coordinates of two endpoints of the bar $\iota^{(i)}$;
$p^{(i)}$: diameter of the bar $\iota^{(i)}$;
$\iota^{(i)}$: the i-th bar of the lattice;
ϖ: the lattice cell consisting of m bars;
Ψ: the overall lattice structure generated from $\mathcal{M}$;
$\tilde{\iota}^{(i)}$: the implicit (level-set) function of the bar $\iota^{(i)}$;
$\widetilde{\varpi}$: the implicit function of the lattice cell ϖ;
$\tilde{\Psi}$: the implicit function of the lattice structure Ψ.

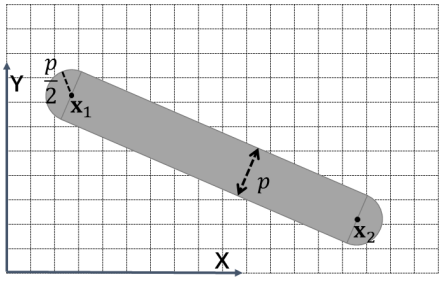

Figure 3: A rod is determined by two nodes $\mathbf{x}_1, \mathbf{x}_2$ and their width p.

The control parameters of the lattice cell include the diameter $\mathbf{p} = (p^{(1)}, p^{(2)}, \ldots, p^{(n)})$ and the endpoint $\mathbf{v} = (\mathbf{v}_1^{(1)}, \mathbf{v}_2^{(1)}, \mathbf{v}_1^{(2)}, \mathbf{v}_2^{(2)}, \ldots, \mathbf{v}_1^{(n)}, \mathbf{v}_2^{(n)})$ of each of its constituent rods. Each bar $\iota^{(i)}$ consists of a cylinder with diameter $p^{(i)}$ and height $\|\mathbf{v}_2^{(i)} - \mathbf{v}_1^{(i)}\|$ and two half-sphere ends with diameter $p^{(i)}$; see Fig. 3. The implicit form $\tilde{\iota}^{(i)}$ of bar $\iota^{(i)}$ is defined as follows,

$$\tilde{\iota}^{(i)}(\mathbf{x}) = \tilde{\iota}(\mathbf{x}, \mathbf{v}_1^{(i)}, \mathbf{v}_2^{(i)}, p^{(i)}) = d(\mathbf{x}, \mathbf{v}_1^{(i)}, \mathbf{v}_2^{(i)}) - \frac{p^{(i)}}{2}, \tag{9}$$

where $d(\mathbf{x}, \mathbf{v}_1, \mathbf{v}_2)$ represents the minimum distance from the point $\mathbf{x}$ to the medial axis of the bar,

$$d(\mathbf{x}, \mathbf{v}_1, \mathbf{v}_2) = \begin{cases} \|\mathbf{b}\|, & \text{if } \mathbf{a}\cdot\mathbf{b} \le 0, \\ \|\mathbf{g}\|, & \text{if } 0 < \mathbf{a}\cdot\mathbf{b} < \mathbf{a}\cdot\mathbf{a}, \\ \|\mathbf{e}\|, & \text{if } \mathbf{a}\cdot\mathbf{b} \ge \mathbf{a}\cdot\mathbf{a}. \end{cases}$$

Here,

$$\begin{array}{llll} \mathbf{a} & = \mathbf{v}_2 - \mathbf{v}_1, & \mathbf{b} & = \mathbf{v} - \mathbf{v}_1, \\ \mathbf{e} & = \mathbf{v} - \mathbf{v}_2, & \mathbf{g} & = (\mathbf{I} - \frac{1}{\|\mathbf{a}\|^2}\mathbf{a}\otimes\mathbf{a})\mathbf{b}. \end{array}$$

Accordingly, the implicit function $\widetilde{\varpi}$ of a lattice cell ϖ is aggregated by the implicit functions $\tilde{\iota}^{(i)}$ $(i = 1, 2, \ldots, n)$ of the n bars. Taking the union of the domains of the bars, that is $\varpi = \cup_{i=1}^{n} \iota^{(i)}$, we have

$$\widetilde{\varpi}(\mathbf{x}, \mathbf{v}, \mathbf{p}) = \max_i \tilde{\iota}(\mathbf{x}, \mathbf{v}_1^{(i)}, \mathbf{v}_2^{(i)}, p^{(i)}).$$

To resolve the issue that the maximum function is not differentiable and to reduce stress concentrations and to improve the bulk modulus, the maximum function is replaced by the Kreisselmeier-Steinhauser (KS) function,

$$\widetilde{\varpi}(\mathbf{x}, \mathbf{v}, \mathbf{p}) = \frac{1}{k} \ln \left(\sum_i^n e^{k\cdot\tilde{\iota}(\mathbf{x}, \mathbf{v}_1^{(i)}, \mathbf{v}_2^{(i)}, p^{(i)})} \right), \tag{10}$$

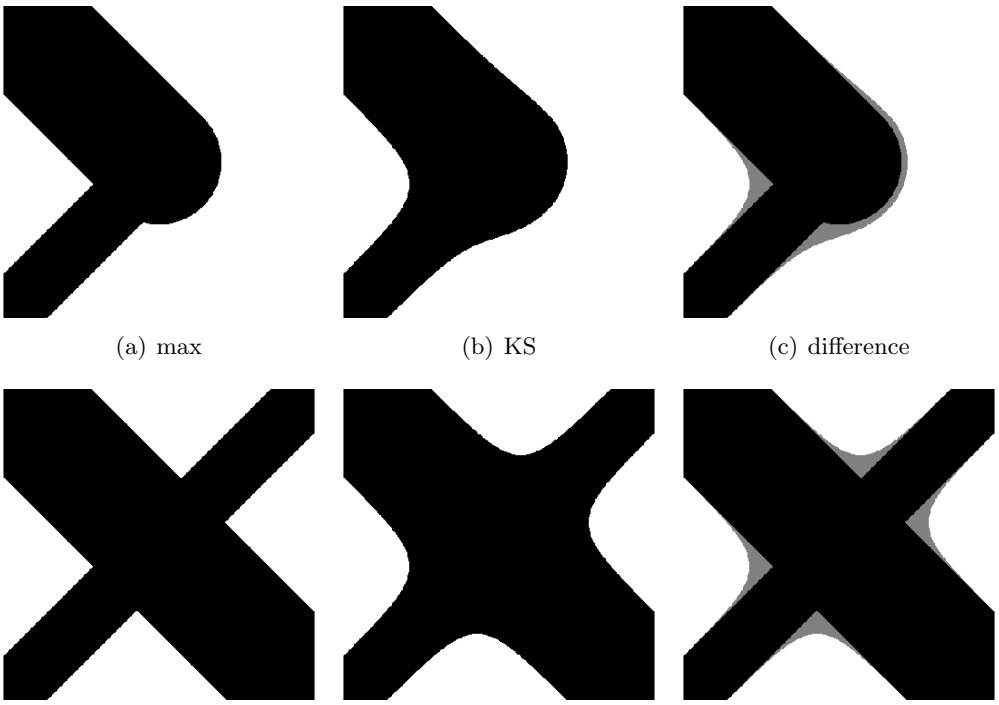

(a) max (b) KS (c) difference

(d) max (e) KS (f) difference

Figure 4: Blending between bars of different widths.

where k is a transition parameter. The different structures obtained using the maximum function and the KS function are illustrated in Fig. 4.

For a finite element (FE) analysis and a uniform expression of the various types of lattice structures, the design geometry is usually projected onto a fixed regular background mesh, described by a density field as follows

$$\boldsymbol{\rho}(\mathbf{x}) = H(\widetilde{\varpi}(\mathbf{x}, \mathbf{v}, \mathbf{p})) \in [0, 1]. \tag{11}$$

H is the heaviside function in a regularized version as

$$H(\widetilde{\varpi}) = \begin{cases} 0, & \Psi > \gamma, \\ -\frac{3}{4}(\frac{\widetilde{\varpi}}{\gamma} - \frac{\widetilde{\varpi}^3}{3\gamma^3}) + \frac{1}{2}, & -\gamma \leq \widetilde{\varpi} \leq \gamma, \\ 1, & \Psi < -\gamma, \end{cases} \tag{12}$$

where γ is a small positive value controlling the magnitude, set as $\gamma = 0.005$ in this study.

Given a solid model Ω and its quadrilateral mesh $\mathcal{M}$, a lattice structure $\Psi(\mathbf{P})$, $\mathbf{P} = \{\mathbf{P}_i\}$, can then be generated by embedding different lattice cells $\mathbf{P}_i = (\mathbf{v}_i, \mathbf{p}_i)$ within each mesh element of $\mathcal{M}$. Following a similar regularization procedure as above, the implicit form $\tilde{\Psi}(\mathbf{P})$ of lattice structure $\Psi(\mathbf{P})$ can then be derived. Under the implicit modeling, the interior and exterior of the lattice cells can be easily determined. It avoids the complex process of meshing and remeshing for FE analysis involved in the optimization iteration process.

The basic lattice cells are generally set with certain periodicity by the users so that the geometric connection and smoothness between neighbouring lattices are kept. They can also be selected from a lattice library with extensive elasticity coverage for wide design choices [51, 52].

4.2. Homogenization and buckling analysis of a lattice cell

The homogenization method is introduced here to establish the averaged macroscopic elastic properties of a microstructure from its local FE analysis [53]. For convenience, the Einstein index summation notation is used here for the basic introduction.

In general, in order to properly describe the buckling performance of a microstructure, a nonlinear theory should be developed, which is however generally too complex to be computed efficiently with high accuracy. In this study, an asymptotic technique is introduced to give a linearized buckling analysis under the assumption of scale separation ([29]), the microstructure is periodically distributed, and its size is relatively much smaller than that of the overall macrostructure.

In the linearized problem, suppose that a microstructure in ω has a small displacement $\mathbf{u}_\omega$ prior to buckling, or moving from an initial displacement $\mathbf{u}^0_\omega$ to a new displacement $\mathbf{u}_\omega$ by a variation $\mathbf{u}^1_\omega$ under an infinitesimal real parameter α, that is,

$$\mathbf{u}_\omega = \mathbf{u}^0_\omega + \alpha \mathbf{u}^1_\omega.$$

From an asymptotic approximation for the displacement $\mathbf{u}^0_\omega$ and $\mathbf{u}^1_\omega$ at an infinitesimal small variation ϵ, we have

$$\begin{aligned} \mathbf{u}^0_\omega(\mathbf{x},\mathbf{y}) &= \mathbf{u}^{00}(\mathbf{x},\mathbf{y}) + \epsilon \mathbf{u}^{01}(\mathbf{x},\mathbf{y}) + \epsilon^2 \mathbf{u}^{02}(\mathbf{x},\mathbf{y}) + \cdots \\ \mathbf{u}^1_\omega(\mathbf{x},\mathbf{y}) &= \mathbf{u}^{10}(\mathbf{x},\mathbf{y}) + \epsilon \mathbf{u}^{11}(\mathbf{x},\mathbf{y}) + \epsilon^2 \mathbf{u}^{12}(\mathbf{x},\mathbf{y}) + \cdots . \end{aligned} \tag{13}$$

Based on the expansion (13), the homogenization theory for the microstructure to predict its effective material property, and its buckling analysis can then be derived following previous studies in [29], as explained below.

The homogenization method is first introduced to predict the averaged effective elasticity tensor (as defined in (3)) to a microstructure built on the assumption of scale separation [53, 54], as stated below.

Lemma 2. *([53, 54]) Given a base cell ω in 2D, D_{ijkl} is the point-by-point varying elasticity tensor on ω. Let $\varepsilon^{0(kl)}_{pq}$ be the prescribed three linearly independent unit test strain fields, specifically, in the horizontal direction (00), in the vertical direction (11), and unit shear strain (01 or 10).*

When only the first order terms of the asymptotic expansion in Eq. (13) *are considered, the effective homogenized elasticity tensor D^H_{ijkl} on the cell ω can be computed as the integral over the average of base cell solution below,*

$$D^H_{ijkl} = \frac{1}{|\omega|} \int_\omega D_{pqrs}(\varepsilon^{0(ij)}_{pq} - \varepsilon^{*(ij)}_{pq})(\varepsilon^{0(kl)}_{rs} - \varepsilon^{*(kl)}_{rs}) \mathrm{d}\omega, \tag{14}$$

where $\varepsilon^{*(ij)}_{pq}$ is the locally varying strain fields defined as

$$\varepsilon^{*(ij)}_{pq} = \varepsilon_{ij}(\boldsymbol{\chi}^{ij}) = \frac{1}{2}(\boldsymbol{\chi}^{ij}_{pq} + \boldsymbol{\chi}^{ij}_{qp}),$$

which are found by solving the elasticity equation at the unit test strain

$$\int_\omega D_{ijkl}\varepsilon_{ij}(\mathbf{v})\varepsilon^{*(ij)}_{pq}\mathrm{d}\omega = \int_\omega D_{ijkl}\varepsilon_{ij}(\mathbf{v})\varepsilon^{0(ij)}_{pq}\mathrm{d}\omega, \quad \forall \mathbf{v} \in V_{\mathbf{y}}, \tag{15}$$

for a virtual displacement field $\mathbf{v}$ in the allowable displacement space $V_{\mathbf{y}}$ and $\mathbf{y}$ is the local coordinate vector in ω.

Eq. (14) is usually approximated in a discrete form by solving Eq. (15) numerically via FE analysis, or,

$$D^H_{ijkl} = \frac{1}{|\omega|}\sum_{e=1}^{N}\int_{\omega_e}(\boldsymbol{\chi}_e^{0(ij)} - \boldsymbol{\chi}_e^{ij})^T\mathbf{k}_e(\boldsymbol{\chi}_e^{0(kl)} - \boldsymbol{\chi}_e^{kl})d\omega_e, \tag{16}$$

for the associated stiffness matrix $\mathbf{k}_e$, or

$$\mathbf{D}^H = \frac{1}{|\omega|}\sum_{e=1}^{N}\int_{\omega_e}(\mathbf{I} - \mathbf{B}\boldsymbol{\chi}_e)^T\mathbf{D}_e(\mathbf{I} - \mathbf{B}\boldsymbol{\chi}_e)d\omega_e,$$

where $\mathbf{I}$ is a 3×3 identity matrix. The term $\mathbf{B}\boldsymbol{\chi}_e$ is taken as the strains caused by the non-homogeneous microstructure within cell ω for the strain-displacement matrix $\mathbf{B}$.

Let $\boldsymbol{\chi}^{kl}$ be the displacement solution on each cell ω corresponding to the test strain field defined in Eq. (15). $\boldsymbol{\chi}^{kl}$ can be derived in a discretized form following classical Galerkin FE analysis by solving the following linear equation system

$$\mathbf{K}^\omega\boldsymbol{\chi}^{kl} = \mathbf{f}_\omega^{kl}, \quad \mathbf{K}^\omega = \sum_{e=1}^{N}\mathbf{K}_{\omega_e},\ k,l = 0,1, \tag{17}$$

for the global stiffness matrix $\mathbf{K}^\omega$ on ω, local stiffnes matrix $\mathbf{K}_{\omega_e}$ for each micro-element ω_e, and load vector $\mathbf{f}_\omega^{kl}$ associated to the test strains on the base cell ω.

Following the analysis in previous study [29] and the first-order asympotic approximation in Eq. (13), the local buckling analysis for a microstructure cell ω is conducted as follows.

Lemma 3. *[29] The first local and periodic eigenmode of a cell ω at the length scale of base cell can be found as eigenvalue solutions to the following equation:*

$$\int_\omega D_{ijkl}(\mathbf{y})\frac{\partial\phi_i}{\partial y_j}\frac{\partial v_k}{\partial y_l}dY + P\int_\omega\left(D_{ijkl}(\mathbf{y}) - D_{ijpq}(\mathbf{y})\frac{\partial\boldsymbol{\chi}_p^{kl}}{\partial y_q}\right)\frac{\partial u_i}{\partial x_j}\frac{\partial\phi_c}{\partial y_k}\frac{\partial v_c}{\partial y_l}dY = 0, \quad \forall\,\mathbf{v}\in V_\mathbf{y}, \tag{18}$$

where P is the eigenvalue (standing for the stability parameter) associated to the buckling mode $\phi_i(\mathbf{y})$, both of which are to be computed. In addition, $\boldsymbol{\chi}$ is the solution to the homogenization problem in Eq. (15) *and* $\mathbf{u}$ *is the macroscopic displacement to the structure after FMO optimization in* (8)*, which together describe the stress values in the cell ω.*

Eq. (18) can also be written as follows,

$$\int_\omega D_{ijkl}(\mathbf{y})\frac{\partial\phi_i}{\partial y_j}\frac{\partial v_k}{\partial y_l}dY + P\int_\omega\sigma_{kl}\frac{\partial\phi_c}{\partial y_k}\frac{\partial v_c}{\partial y_l}dY = 0, \quad \forall\,\mathbf{v}\in V_\mathbf{y}.$$

Accordingly, following a discretized FE analysis process, the buckling load factor P and the corresponding buckling mode vector $\boldsymbol{\phi}$ are obtained by computing solution to the following eigenvalue problem,

$$[\mathbf{K}^\omega(\mathbf{p}) - P\mathbf{G}(\boldsymbol{\chi},\mathbf{p})]\,\boldsymbol{\phi} = 0,$$

where $\mathbf{K}^\omega$ is the stiffness matrix in computing $\boldsymbol{\chi}$ in Eq. (15) in a form as (17), and $\mathbf{G}$ is the global geometric stiffness matrix for displacement $\boldsymbol{\chi} = \{\boldsymbol{\chi}_e^{kl}\}$ defined as

$$\mathbf{G} = -\sum_{e=1}^{N}\int_{\omega_e}\left(\frac{\partial\mathbf{N}}{\partial y_k}\right)^{\mathrm{T}}(\sigma_{kl})_e\left(\frac{\partial\mathbf{N}}{\partial y_l}\right)d\omega \tag{19}$$

for the finite element shape function $\mathbf{N}(\mathbf{y})$ in ω and the stress load $\boldsymbol{\sigma}_e$ whose computation is further explained below. The eigenvector is normalized as $\boldsymbol{\phi}^{\mathrm{T}}\mathbf{K}^{\omega}(\mathbf{p})\boldsymbol{\phi} = 1$ by assuming a distinct eigenvalue. Note here these definitions are implicitly dependent on the design parameter $\mathbf{p}$. Properly designing the optimal microstructures under buckling constraint will involve computing their derivatives with respect to the design variables $\mathbf{p}$, as will be explained in Section 5.

The stress $\boldsymbol{\sigma}_e$ per micro-element e in Eq. (19) is computed as follows. After clustering the macroscale elasticity tensors, each class of materials has different local stresses in different locations. The element with the largest von Mises stress value in one class is selected and its associated strain is set to be the local strain load $\bar{\boldsymbol{\varepsilon}}$ determined by

$$\bar{\boldsymbol{\varepsilon}} = \mathbf{D}_0^{-1}\bar{\boldsymbol{\sigma}},$$

for the target elasticity tensor $\mathbf{D}_0$.

Consequently, the stress $\boldsymbol{\sigma}_e$ for each micro-element e is calculated by

$$\boldsymbol{\sigma}_e = \mathbf{D}_e(\mathbf{I} - \mathbf{B}\boldsymbol{\chi}_e)\bar{\boldsymbol{\varepsilon}}, \tag{20}$$

where $\mathbf{B}$ is the strain-displacement matrix, $\boldsymbol{\chi}_e$ is the displacement derived via Eq. (15).

The above numerical approach is set up based on the hypothesis that the microscale displacements are periodic, and that the buckling mode is restricted within a single macro-element. In cases the assumptions are not satisfied, other advanced approaches can be applied to improve the analysis accuracy and structural stability. For example, Zeman et al have proposed the quasicontinuum method for analysis of elastic and dissipative properteis of quasi-periodic lattice structures [55, 56, 57, 58]. Li and Hu [59] proposed to construct material-aware shape functions for analysis of heterogeneous structures with no assumption of scale separations. In case that the buckling mode spans more than one elements, the Bloch-Floquet theory based approaches have to be adopted, as have been conducted in a series of excellent work [29, 34, 36, 37, 38]. The topics are however not the present research focus, and is to be explored in our future work.

5. Inverse microstructure design under buckling constraint

The goal of the micro-optimization stage is to obtain a microstructure with desirable physical properties, specifically, to match the elasticity tensor obtained under additional buckling constraints. We also mention that previous studies such as [35, 39, 29] have dealt with the topological optimization problem of minimizing the compliance under buckling constraints. These studies are further extended to microstruture matching under buckling constraint.

5.1. Inverse lattice design under buckling constraints

The topology optimization of inverse microstructure design under buckling constrains is formulated as follows,

$$\begin{aligned}
\min_{\mathbf{p}\in\mathbb{P}} \quad & J = ||\mathbf{D}^H(\mathbf{p}) - \mathbf{D}_0||_F && s.t. \\
& \mathbf{K}^{\omega}(\mathbf{p})\boldsymbol{\chi}^{kl} = \mathbf{f}^{kl}, && k,l = 0,1, \\
& V(\mathbf{p}) \le V^*, && \\
& \left[\mathbf{K}^{\omega}(\mathbf{p}) - P\mathbf{G}(\boldsymbol{\chi},\mathbf{p})\right]\boldsymbol{\phi} = 0, && \\
& P_j \ge \underline{P}, && j \in J_b,
\end{aligned} \tag{21}$$

where $\mathbf{D}_0$ is the desired elasticity tensor, $\mathbf{p}$ is the design variable of bar radii in the admissible space $\mathbb{P}$, $\mathbf{D}^H(\mathbf{p})$ is the homogenized elasticity tensor defined by Eq. (16). In addition, $\mathbf{K}^\omega(\mathbf{p})$ is the global stiffness matrix corresponding to design $\mathbf{p}$, $\boldsymbol{\chi}^{kl}$ is the vector of the nodal displacements to be computed and $\mathbf{f}^{kl}$ is the external loadings of the test cases (kl), V^* is the desired volume fraction, $V(\mathbf{p})$ is the volume of design $\mathbf{p}$, P_j is the j-th eigenvalue in the eigenvalue set J_b, and $\underline{P}$ is the prescribed lower bound of eigenmode.

Properly addressing the optimization problem in Eq. (21) of continuum structures considering eigenvalues meet with several severe challenges. Firstly, the large number of buckling constraints $P_j \geq \underline{P}$ may deteriorate the optimization convergence. In addition, mode switching and multimode can appear during the optimization process, which may cause difficulties in sensitivity analysis of eigenvalues. Particularly the repeated eigenvalues associated with multimode are non-differentiable.

To circumvent the difficulty, the following single constraint equation is used to replace the last buckling constraint in Eq. (21)

$$f(P) = \kappa^{KS}\underline{P} - 1 \leq 0, \tag{22}$$

or

$$\kappa^{KS} \leq \frac{1}{\underline{P}}, \tag{23}$$

where κ^{KS} is a K-S aggregation function defined below

$$\kappa^{KS} = \kappa_1 + \frac{1}{\mu_\kappa} \ln \left[\sum_{j \in J_b^*} \exp(\mu_\kappa(\kappa_j - \kappa_1)) \right],$$

in which

$$\kappa_j = \frac{1}{P_j}, \qquad \mu_\kappa = \frac{100}{\kappa_1}$$

for the j-th eigenvalue P_j, and an aggregation parameter μ_κ, and J_b^* is a subset of J_b containing only indices of the first n_b buckling modes.

In case the eigenvalue is too small, the aggregation function is also scaled by the following parameter to improve the iteration convergence,

$$c_b = \frac{\kappa_1}{\kappa^{KS}}.$$

Taking into account of the above discussions, the microscopic inverse design problem under buckling constraint in Eq. (21) is re-formulated as

$$\begin{aligned} \min_{\mathbf{p}\in\mathbb{P}} \quad & O(\mathbf{p}) = (1-\lambda^B)||\mathbf{D}^H(\mathbf{p}) - \mathbf{D}_0||_F + \lambda^B \kappa^{KS} \quad s.t. \\ & \mathbf{K}^\omega(\mathbf{p})\boldsymbol{\chi}^{kl} = \mathbf{f}^{kl}, \quad k,l = 0,1, \\ & V(\mathbf{p}) \leq V^*, \\ & [\mathbf{K}^\omega(\mathbf{p}) - P\mathbf{G}(\boldsymbol{\chi},\mathbf{p})]\,\boldsymbol{\phi} = 0, \\ & f(P) = \kappa^{KS}\underline{P} - 1 \leq 0, \end{aligned} \tag{24}$$

where λ^B is the weight of the pre-specified buckling constraint, and the last inequality is defined in Eq. (22).

Note here the original formulation in (21) must handle a large number of buckling constraints, which involves huge computational efforts. By employing a single aggregated KS functions to

approximate the maximum buckling mode [39], the costs are tremendously reduced. On the other hand, it also introduces approximation errors such that the maximum buckling mode are not accurately controlled.

In addition, for the low-density region during optimization, the problem of pseudo buckling modes may occur. The adaptive continuation method of Gao [60] is taken to overcome it.

5.2. Numerics and sensitivities

Computing solution to the inverse homogenization problem (21) is very challenging due to the inclusion of the nonlinear objective and constraint functions, which results in an overall complex nonlinear and nonconvex optimization problem. The well-established optimization approach Globally Convergent Method of Moving Asymptotes (GCMMA) [61] is applied here to resolve the issue. It approximates the original nonconvex problem through a set of convex sub-problems by using the gradients of the optimization objective and constraints with respect to the design variables.

As described in Section 4.1, we first project the lattice microstructure onto the density field and then perform the finite element analysis. Here, a modified solid isotropic material with penalization (SIMP) format is used to interpolate the intrinsic property E between the hollow and solid elements,

$$E(\rho) = \begin{cases} E_{\min} + \rho^p (E_0 - E_{\min}) & for\ \mathbf{K}^\omega, \mathbf{f}, \\ \rho^p E_0, & for\ \mathbf{G}, \end{cases} \tag{25}$$

where p is a penalization factor, $E_{\min}$ is the relative density of the void phase which is set to a small value to avoid numerical singularities, and E_0 is the constitutive tensor of the solid phase.

The modified scheme is used to eliminate the notoriously known problem of artificial modes which contaminate low-density regions. To ensure the scheme's success, the value of $E_{\min}$ must be large enough to stabilize low-density regions while still being small enough to have negligible influence on the bifurcation loads. Through multiple numerical studies, $E_{\min} = 10^{-4} E_0$ was found to yield the best results without causing significant alterations of the loads.

In solving the microscale lattice design using GCMMA, the approach mainly depends on computation of the derivatives of the objective and constraint functions, or called sensitivity analysis. Different from the density-based topology optimization, the design variables of the microstructure optimization are the widths of the bars instead of the discretized density field. The sensitivities of the objective and constraint functions with respect to the design variables are computed via the chain rule as follows

$$\frac{df(\mathbf{p})}{d\mathbf{p}} = \frac{\partial f(\mathbf{p})}{\partial \rho} \frac{\partial \rho}{\partial \mathbf{p}}, \tag{26}$$

where $f(\mathbf{p})$ represents the objective function or the constraint functions.

Firstly, the gradients of the density field with respect to the design variables $\partial\rho/\partial\mathbf{p}$ can be derived from Eqs. (9), (10), and (12) as

$$\frac{\partial \rho}{\partial p^{(i)}} = \frac{\partial H(\Psi(\mathbf{p}))}{\partial p^{(i)}} = \frac{\partial H}{\partial \Psi} \frac{\partial \Psi(\mathbf{p})}{\partial p^{(i)}},$$

where

$$\frac{\partial H}{\partial \Psi} = \begin{cases} \frac{3(\varepsilon-1)(\Psi^2-\gamma^2)}{4\gamma^3}, & -\gamma \le \Psi \le \gamma, \\ 0, & \Psi < -\gamma \text{ or } \Psi > \gamma, \end{cases}$$

$$\frac{\partial \Psi(\mathbf{p})}{\partial p^{(i)}} = -\frac{\exp(-k(d^{(i)} - \frac{p^i}{2}))}{\sum_{j=1}^{n} \exp(-k(d^j) - \frac{p^{(j)}}{2})}. \tag{27}$$

The gradients of $V = \sum_e \rho_e$, J in Eq. (21), $f(P)$ in Eq. (22) with respect to the density field ρ, or $\partial V/\partial \rho_e$, $\partial J/\partial \rho_e$ and $\partial f(P)/\partial \rho_e$ are derived below.

The derivatives of the volume constraint V with respect to density ρ_e are given by

$$\frac{\partial V(\boldsymbol{\rho})}{\partial \rho_e} = \frac{\partial(\sum_e \boldsymbol{\rho}_e)}{\partial \rho_e} = 1.$$

The derivatives of the objective function $J = ||\mathbf{D}^H(\mathbf{p}) - \mathbf{D}_0||_F$ in Eq. (21) with respect to density ρ_e are given by

$$\frac{\partial J}{\partial \rho_e} = \frac{\partial J}{\partial \mathbf{D}^H}\frac{\partial \mathbf{D}^H}{\partial \rho_e}, \tag{28}$$

where

$$\begin{aligned}
\frac{\partial J}{\partial \mathbf{D}^H} &= \mathrm{Tr}((\mathbf{D}^H(\boldsymbol{\rho}) - \mathbf{D}^0)^T(\mathbf{D}^H(\boldsymbol{\rho}) - \mathbf{D}^0))^{(-\frac{1}{2})}(\mathbf{D}^H(\boldsymbol{\rho}) - \mathbf{D}^0), \\
\frac{\partial D^H_{ijkl}}{\partial \rho_e} &= \frac{1}{|\omega|} p\rho_e^{p-1}\left(E_0 - E_{\min}\right)\left(\boldsymbol{\chi}_e^{ij}\right)^T \mathbf{k}_0 \boldsymbol{\chi}_e^{kl}.
\end{aligned}$$

The derivative of the buckling constraint $f(P)$ defined in Eq. (22) with respect to ρ_e can be expressed as

$$\frac{\partial f(P)}{\partial \rho_e} = \underline{P}\frac{\partial \kappa^{KS}}{\partial \rho_e} = \frac{\underline{P}}{\sum_{j\in J_b^*}\exp(\mu_\kappa \kappa_j)}\sum_{j\in J_b^*}\exp(\mu_\kappa\kappa_j)\frac{\partial \kappa_j}{\partial \rho_e}.$$

Following previous studies [28, 29], we now explain below the approach to derive the derivative of the critical load factor κ_j with respect to the density ρ_e under the assumption that all eigenvalues P are positive.

First, consider the case that the eigenvalue κ_j is unimodal. Following its definition,

$$\frac{1}{P} = \max_{\boldsymbol{\phi}} \frac{\boldsymbol{\phi}^T \mathbf{G} \boldsymbol{\phi}}{\boldsymbol{\phi}^T \mathbf{K}^\omega \boldsymbol{\phi}}. \tag{29}$$

For each specific instability mode ϕ, we have from [29] the associated gradients based on an adjoint approach. Specifically, by setting $11 \to 1$, $22 \to 2$ and $12 \to 3$ for ease of explanation, we have

$$\frac{\partial \kappa_j}{\partial \rho_e} = \boldsymbol{\phi}_j^{\mathrm{T}}\left(\frac{\partial \mathbf{G}}{\partial \rho_e} - \kappa_j \frac{\partial \mathbf{K}^\omega}{\partial \rho_e}\right)\boldsymbol{\phi}_j - \sum_{k=1}^{3}\left(\mathbf{v}_j^k\right)^{\mathrm{T}}\left(\frac{\partial \mathbf{K}^\omega}{\partial \rho_e}\boldsymbol{\chi}^k - \frac{\partial \mathbf{f}^k}{\partial \rho_e}\right), \tag{30}$$

where $\mathbf{v}_j^k$ is an adjoint vector with respect to the jth buckling mode, obtained by solving the following adjoint equation for load $k = 1, 2, 3$ and buckling modes $\boldsymbol{\phi}_j$, $j = 1, .., n_b$,

$$\mathbf{K}^\omega \mathbf{v}_j^k = \mathbf{P}_j^k, \tag{31}$$

where the right-hand-side vector $\mathbf{P}_j^k$ is given as,

$$\begin{aligned}
\mathbf{P}_j^k &= (\boldsymbol{\phi}_j^k)^{\mathrm{T}}\frac{\partial \mathbf{G}}{\partial \boldsymbol{\chi}^k}\boldsymbol{\phi}_j^k \\
&= \sum_{e=1}^{N}\left\{(\boldsymbol{\phi}_{j,e}^k)^{\mathrm{T}}\frac{\partial \mathbf{G}_e}{\partial \boldsymbol{\chi}_{e,1}^k}\boldsymbol{\phi}_{j,e}^k, \cdots, (\boldsymbol{\phi}_{j,e}^k)^{\mathrm{T}}\frac{\partial \mathbf{G}_e}{\partial \boldsymbol{\chi}_{e,8}^k}\boldsymbol{\phi}_{j,e}^k\right\}^{\mathrm{T}}
\end{aligned}$$

with

$$\frac{\partial \mathbf{G}_e}{\partial \chi_{e,i}^k} = -\int_{Y_e} \left(\frac{\partial N}{\partial y_l}\right)^{\mathrm{T}} \frac{\partial (\sigma_{lm})_e}{\partial \chi_{e,i}^k} \left(\frac{\partial N}{\partial y_m}\right) dY.$$

We have from Eq. (20),

$$\frac{\partial \boldsymbol{\sigma}_e}{\partial \chi_{e,i}^k} = -E_e \mathbf{B}\mathbf{e}_{ik}\bar{\boldsymbol{\varepsilon}}, \qquad i = 1, \cdots, 8.$$

The derivatives of the global stiffness matrices $\mathbf{K}^\omega$, $\mathbf{G}$ and loads $\mathbf{f}^k$ are calculated by

$$\begin{aligned} \frac{\partial \mathbf{K}^\omega}{\partial \rho_e} &= p(1 - E_{\min}/E_0)\rho_e^{p-1}\mathbf{k}_e^0, \\ \frac{\partial \mathbf{G}}{\partial \rho_e} &= p\rho_e^{p-1}\mathbf{G}_e^0, \\ \frac{\partial \mathbf{f}^k}{\partial \rho_e} &= p(1 - E_{\min}/E_0)\rho_e^{p-1}\mathbf{f}_e^{0k}, \end{aligned}$$

where $\mathbf{k}_e^0$, $\mathbf{G}_e^0$, $\mathbf{f}_e^{0k}$ are element matrices and vectors evaluated with the constitutive matrix of the solid phase E_0. More details on the derivations are referred to [28, 29].

Accordingly, we have the following results on the derivatives about the design objective in the optimization problem in Eq. (24).

Lemma 4. *The derivatives of the optimization target in Eq.* (24)*, or,*

$$O(\mathbf{p}) = (1 - \lambda^B)||\mathbf{D}^H(\mathbf{p}) - \mathbf{D}_0||_F + \lambda^B \kappa^{KS}$$

is given as

$$\frac{\partial O(\mathbf{p})}{\partial \mathbf{p}} = \frac{\partial O(\mathbf{p})}{\partial \boldsymbol{\rho}} \frac{\partial \boldsymbol{\rho}}{\partial \mathbf{p}},$$

where $\partial \boldsymbol{\rho}/\partial \mathbf{p}$ *is given in* (27) *and*

$$\frac{\partial O(\mathbf{p})}{\partial \boldsymbol{\rho}} = (1 - \lambda^B)\frac{\partial J(\mathbf{p})}{\partial \boldsymbol{\rho}} + \lambda^B \frac{\partial \kappa^{KS}}{\partial \boldsymbol{\rho}},$$

where the two derivatives on the right are given in Eqs. (28) *and* (30)*, and* $p^{(i)}$ *is a component of the bar radius vector* $\mathbf{p}$*.*

More concrete details on computation of the derivatives are described in Algorithm 1.

5.3. Post-processing

The inverse design problem described above is solved on every group of clustered elasticity tensors to generate the desired microstructure. Due to the scale separation of the homogenization and the individual optimization of each microstructure, the microstructure obtained by solving the aforementioned optimization problem may have structures that do not meet the actual manufacturing requirements, for example, the rods in a single microstructure are too thin, or adjacent microstructures are not connected when they are combined together as a whole. These issues are addressed by the following post-processings.

Algorithm 1: Sensitivity of buckling constraint functions

Input: x, p, ρ_{min}, n_b, $\boldsymbol{\chi}$, $\bar{\mathbf{E}}$, $d\bar{\mathbf{E}}$, $optMacroConstrain$, $valMacroConstrain$
Output: $\{\frac{\partial f(P)}{\partial \rho_e}\}_{e=1}^{N}$

// Compute the objective function

$f(P) = \underline{P}\kappa^{KS} - 1 \le 0,\ \kappa^{KS} = \kappa_1 + \frac{1}{\mu_\kappa}\ln\left[\sum_{j\in J_b^*}\exp(\mu_\kappa(\kappa_j-\kappa_1))\right],\ \kappa_j = \frac{1}{P_j},\ c_b = \frac{\kappa_1}{\kappa^{KS}},\ \mu_\kappa = 100/\kappa_1$

// Compute adjoint vectors

for *buckling modes* $j = 1, \cdots, n_b$ **do**
  for *load* $k = 1, 2, 3$ **do**
    for *micro-element* $e = 1, \cdots, N$ **do**
      for *degree of freedom* $i = 1, \cdots, 8$ **do**
        Compute $\frac{\partial \mathbf{G}_e}{\partial \chi_{e,i}^k}$ by

$$\frac{\partial \mathbf{G}_e}{\partial \chi_{e,i}^k} = -\int_{Y_e}\left(\frac{\partial \mathbf{N}}{\partial y_l}\right)^{\mathrm{T}}\frac{\partial(\sigma_{lm})_e}{\partial \chi_{e,i}^k}\left(\frac{\partial \mathbf{N}}{\partial y_m}\right)^{\mathrm{T}}dY, \quad \frac{\partial \boldsymbol{\sigma}_e}{\partial \chi_{e,i}^k} = -\mathbf{E}_e\mathbf{B}_e\mathbf{e}_{ik}\bar{\boldsymbol{\varepsilon}}, \tag{32}$$

    Compute $\mathbf{P}_j^k$ by

$$\mathbf{P}_j^k = (\boldsymbol{\phi}_j^k)^{\mathrm{T}}\frac{\partial \mathbf{G}}{\partial \boldsymbol{\chi}^k}\boldsymbol{\phi}_j^k = \sum_{e=1}^{N}\left\{(\boldsymbol{\phi}_{j,e}^k)^{\mathrm{T}}\frac{\partial \mathbf{G}_e}{\partial \boldsymbol{\chi}_{e,1}^k}\boldsymbol{\phi}_{j,e}^k, \cdots, (\boldsymbol{\phi}_{j,e}^k)^{\mathrm{T}}\frac{\partial \mathbf{G}_e}{\partial \chi_{e,8}^k}\boldsymbol{\phi}_{j,e}^k\right\}^{\mathrm{T}} \tag{33}$$

    Compute v_j^k by solving $K^\omega v_j^k = P_j^k$

// Compute sensitivities for each element

for *element* $e = 1, \cdots, N$ **do**
  Get displacement $\boldsymbol{\chi}_e$ and compute $\frac{\partial \mathbf{G}}{\partial \rho_e}$ and $\frac{\partial \mathbf{K}}{\partial \rho_e}$ by

$$\frac{\partial \mathbf{G}}{\partial \rho_e} = p\rho_e^{p-1}\mathbf{G}_e^0, \quad \frac{\partial \mathbf{K}}{\partial \rho_e} = p(1-E_{\min}/E_0)\rho_e^{p-1}\mathbf{K}_e^0, \tag{34}$$

  switch *optMacroConstrain* **do**
    case *Stress* **do**
      Compute $\frac{\partial \mathbf{G}_e}{\partial \bar{\boldsymbol{\varepsilon}}}\frac{\partial \bar{\boldsymbol{\varepsilon}}}{\partial \rho_e}$ by

$$\frac{\partial \mathbf{G}}{\partial \bar{\varepsilon}_k} = -\sum_{e=1}^{N}\int_{Y_e}\left(\frac{\partial \mathbf{N}}{\partial y_l}\right)^{\mathrm{T}}\frac{\partial(\sigma_{lm})_e}{\partial \bar{\varepsilon}_k}\left(\frac{\partial \mathbf{N}}{\partial y_m}\right)^{\mathrm{T}}dY, \quad \frac{\partial \boldsymbol{\sigma}_e}{\partial \bar{\varepsilon}_k} = \mathbf{E}_e(\mathbf{I}-\mathbf{B}_e\boldsymbol{\chi}_e)\mathbf{e}_k,\ \bar{\mathbf{E}}\frac{\partial \bar{\boldsymbol{\varepsilon}}}{\partial \rho_e} = -\frac{\partial \bar{\mathbf{E}}}{\partial \rho_e}\bar{\boldsymbol{\varepsilon}} \tag{35}$$

    case *Strain* **do**
      Compute $\frac{\partial \mathbf{G}_e}{\partial \bar{\boldsymbol{\varepsilon}}}\frac{d\bar{\boldsymbol{\varepsilon}}}{d\rho_e} = 0.$
  $T_0 \longleftarrow 0;$
  for *buckling modes* $j = 1, \cdots, n_b$ **do**
    Compute $\kappa_j,\ \boldsymbol{\phi}_{j,e}$
    $T_1 \longleftarrow 0;$
    for *load* $k = 1, 2, 3$ **do**
      Compute $\frac{\partial \mathbf{f}^k}{\partial \rho_e} = p(1-E_{\min}/E_0)\rho_e^{p-1}\mathbf{f}_e^{0k}.$
      Update $T_1 = T_1 + (\mathbf{v}_{j,e}^k)^{\mathrm{T}}\left(\frac{\partial \mathbf{K}_e}{\partial \rho_e}\boldsymbol{\chi}_e^k - \frac{\partial \mathbf{f}_e^k}{\partial \rho_e}\right)$
    Compute

$$\frac{\partial \kappa_j}{\partial \rho_e} = \boldsymbol{\phi}_{j,e}^{\mathrm{T}}\left(\frac{\partial \mathbf{G}}{\partial \rho_e} + \frac{\partial \mathbf{G}}{\partial \bar{\boldsymbol{\varepsilon}}}\frac{\partial \bar{\boldsymbol{\varepsilon}}}{\partial \rho_e} - \kappa_j * \frac{\partial \mathbf{K}}{\partial \rho_e}\right)\boldsymbol{\phi}_{j,e} - T_1 \tag{36}$$

    Compute $\sum_{j\in J_b^*}\exp(\mu_\kappa\kappa_j)\frac{\partial \kappa_j}{\partial \rho_e}$ by $T_0 = T_0 + \exp(\mu_\kappa\kappa_j) * \frac{\partial \kappa_j}{\partial \rho_e}$
  Compute $\frac{\partial f(P)}{\partial \rho_e} = \underline{P}\frac{\partial \kappa^{KS}}{\partial \rho_e} = \frac{\underline{P}}{\sum_{j\in J_b^*}\exp(\mu_\kappa\kappa_j)} * T_0$

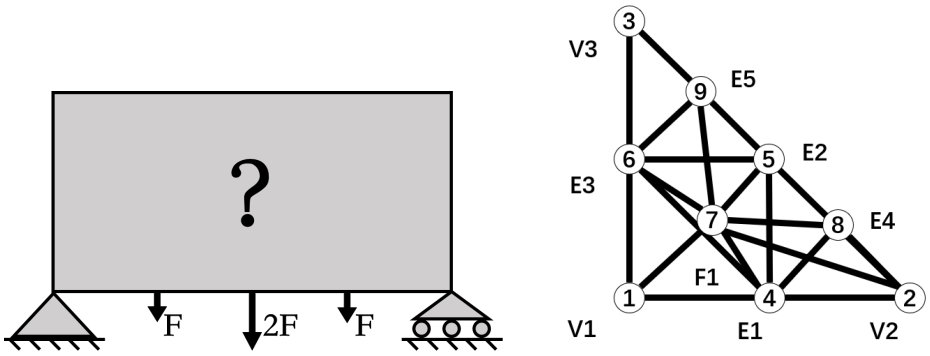

(a) The bridge design problem (b) One-eighth of the basic model

Figure 5: The bridge lattice design problem. The basic model of the one-eighth lattice microstructure using 21 rods determined by 9 points as design variables, where the appearance and thickness of each rod is determined by optimization.

Firstly, check structural manufacturability on the over-thin rods, and remove them to reduce potential manufacturing failure. After the operation, the structural connectivity must be checked again against its neighboring four cells. Excess suspended rods are removed. Secondly, after completing the above two-stage optimization procedures, the radii of the derived rods are optimized again to strictly meet the volume constraint. Thirdly, for two disconnected adjacent cells, the two rods with the closest endpoint distance are connected at their endpoints by adding a new rod between them.

6. Examples

The method has also been implemented on MATLAB 2017b on a PC of Intel Core i5-4590 3.2GHz CPU and 16GB RAM. The FMO problem is solved by calling MOSEK 9.1 through YALMIP [62]. The linear objective function and constraints other than the buckling problem have a good mathematical structure, but introduce additional large-scale matrix inequalities whose computation is very time-consuming and requires a lot of memory resources, for which the method in reference [63] can also be used. In all examples, the inverse homogenization problem (21) has a design domain of size 50×50 with micro-element of length 1. Microstructures consist of Poisson's ratio $\nu = 0.3$, Young's modulus $E_0 = 1$, $E_{min} = 0.1^3$ of the material. The macroscopic and each microscopic volume constraint is uniformly set to 0.35 in the study.

6.1. Bridge design problem

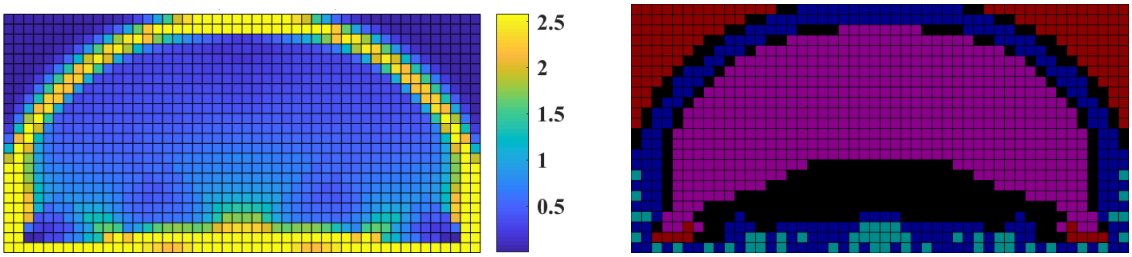

(a) The result of macroscopic optimization in a continuous free isotropic space, $c = 1.4618$.

(b) The result after clustering, $c = 1.5899$. The number of clusters is 5.

Figure 6: Macro-optimization results for the first step of the bridge problem.

The approach's performance for multi-lattice structure design under buckling constraints was first tested on the classical bridge problem shown in Fig. 5(a). The macro- design domain was divided into 48×24 cells, the external loading was 0.1, the volume fraction was 0.35, and the number of clusters was set to 5.

The base lattice microstructure to be optimized was shown in Fig. 5(b). Its one-eighth part has 21 rods determined by 3 vertices, 5 edge points, 1 face point, which 9 points were taken as design variables. Considering that we are using a symmetric design strategy for the one-eighth lattice, we optimized the macroscopic problem in an isotropic material space.

Fig. 6(a) showed the final optimized lattice structure of a resulted compliance $c = 14.618$. The different distributed elasticity tensors were further clustered to produce a structure consisting of five types of different materials, whose compliance become $c = 15.899$, as given in Fig. 6(b).

Based on the above results, different microstructures corresponding to the five types of material elasticity tensors were designed separately using an inverse design strategy. The associated results were shown in Fig. 7, under different weights λ^B of buckling constraint, respectively of $0, 0.01, 0.02, 0.4$, and 0.9 for purpose of wide testing.

Structural compliance obtained by the above two-scale optimization process were in sequence 19.6117, 14.0077, 23.9039, 24.9216 and 11.4800 for these different tests. It can be seen that the overall structural performances did not decrease monotonically with the introduction of the local buckling constraint. It may partially come from the microscopic inverse design problem formulation in Eq. (21), which no longer considers the overall structural compliance. A simultaneous macro- and micro- topology optimization under buckling constraint may help resolve the issue, as studied in [38], which are to be further explored in our future work.

6.2. Inverse design of microstructures

Performance of the method on design optimization of a singe microstructure with desired elasticity tensor under different buckling constraints was further tested here, still taking as example the bridge design problem in Section 6.1.

Fig. 8 shows the optimization results of six types of lattice microstructures at different locations or conditions of the macro-domain, where a single lattice cell, its four-cell tiling at a 60×60 resolution were respectively shown in the left and right figure. In order to test the method's performance in handling connections between adjacent microstructures, the resulted cells are further

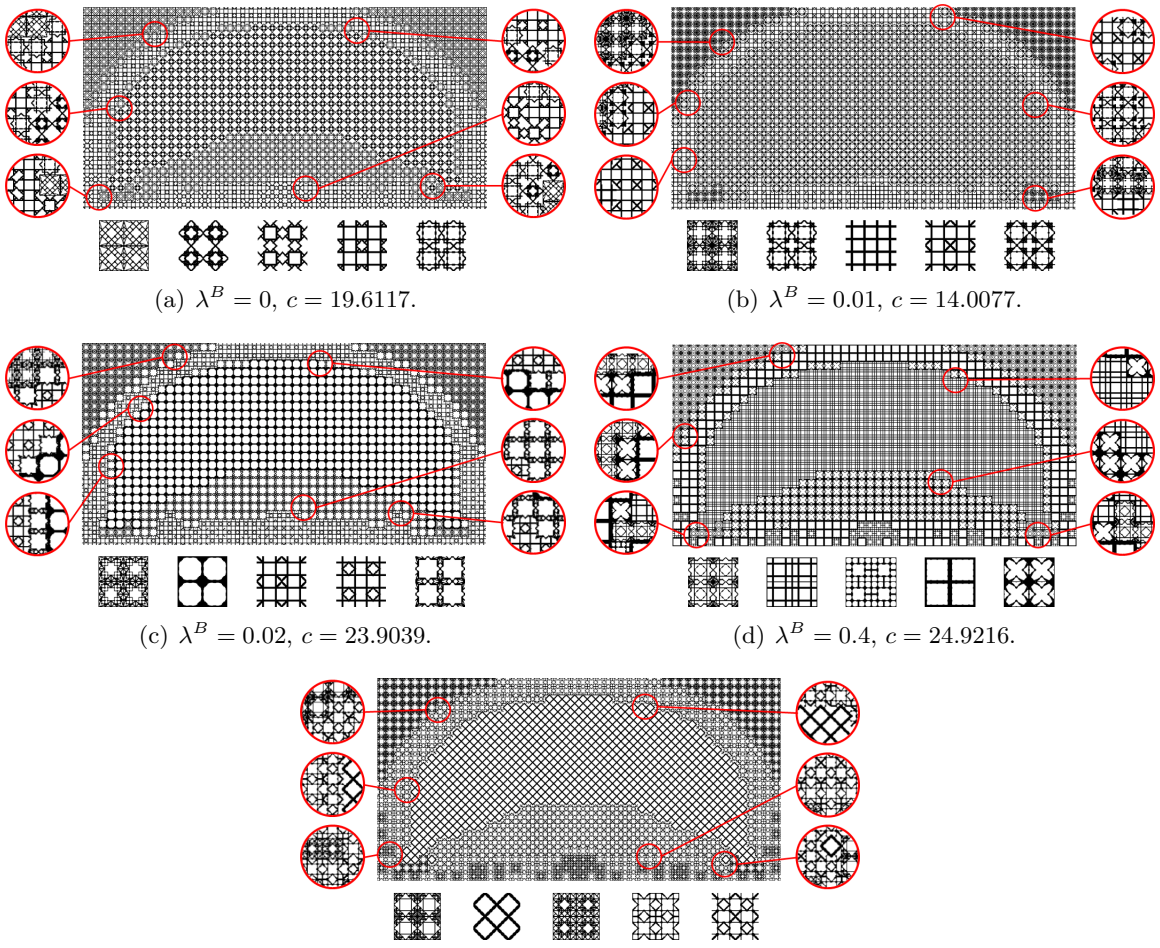

(a) $\lambda^B = 0$, $c = 19.6117$. (b) $\lambda^B = 0.01$, $c = 14.0077$.

(c) $\lambda^B = 0.02$, $c = 23.9039$. (d) $\lambda^B = 0.4$, $c = 24.9216$.

(e) $\lambda^B = 0.9$, $c = 11.4800$.

Figure 7: Optimization results of the bridge problem.

stitched together following the approach in Section 5.3. Fig. 9 showed some connection examples of structure (a) and structure (b) in Fig. 8. It can be seen that the scheme can ensure continuity when connecting different microstructures.

The iteration histories in the inverse design of microstructures under buckling constraint were also plotted in Figs. 10 and 11 for two typical microstructures in Figs. 7(d), and 8(e). The variations of the design target $O(\mathbf{p})$, volume fraction $V(\mathbf{p})$, buckling constraint $f(\lambda)$ and the first and third eigenvalues P_1, P_3 were plotted respectively; See also the problem formulation in Eq. (24). The iterations were not varying smoothly but still ultimately reached the expected values.

Accuracy of our buckling analysis was also tested in comparison with those from commercial software ANASYS. Given two bucking modes $\boldsymbol{\chi}_1, \boldsymbol{\chi}_2$ computed from different approaches, the Cosine similarity for them is defined to measure their approximation,

$$s(\boldsymbol{\chi}_1, \boldsymbol{\chi}_2) = cos(\theta(\boldsymbol{\chi}_1, \boldsymbol{\chi}_2)) = \frac{\boldsymbol{\chi}_1 \cdot \boldsymbol{\chi}_2}{\|\boldsymbol{\chi}_1\| \, \|\boldsymbol{\chi}_2\|} = \frac{\sum_{i=1}^{n} \chi_1^i \chi_2^i}{\sqrt{\sum_{i=1}^{n} (\chi_1^i)^2} \sqrt{\sum_{i=1}^{n} (\chi_2^i)^2}}. \tag{37}$$

Clearly, the more close approximate to 1.0 $s(\boldsymbol{\chi}_1, \boldsymbol{\chi}_2)$ is, the more similar the two eigenmodes $\boldsymbol{\chi}_1, \boldsymbol{\chi}_2$

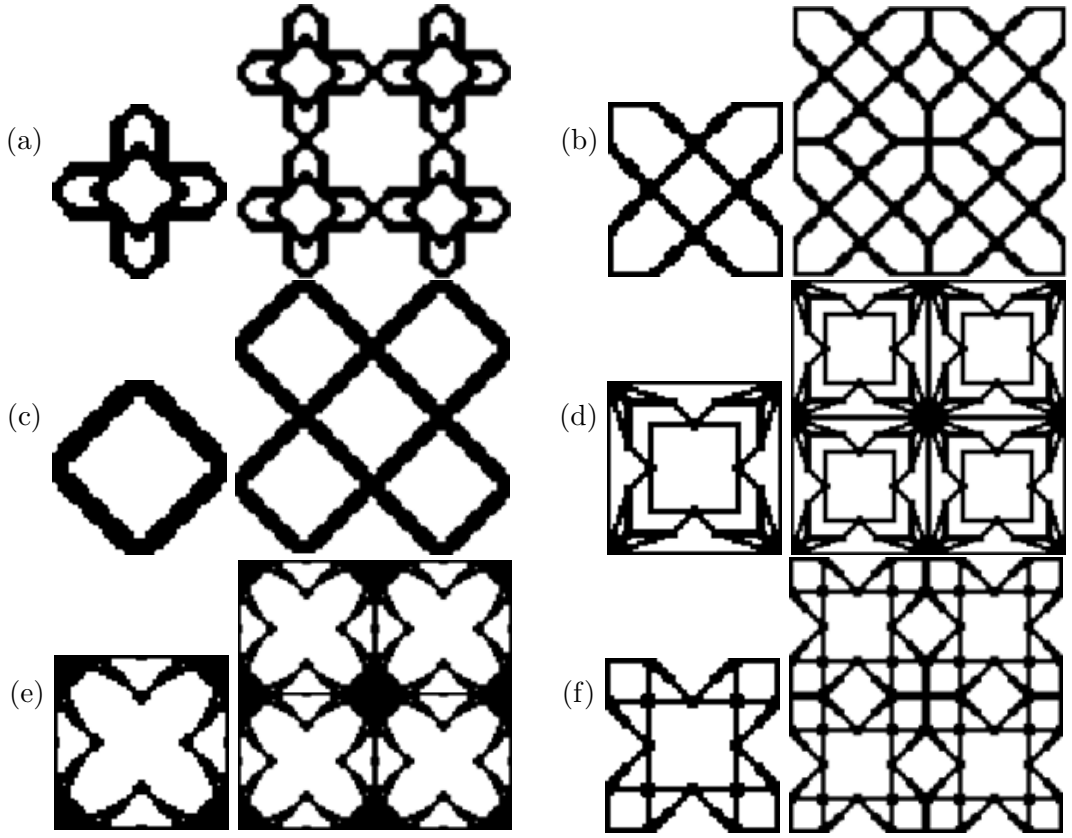

Figure 8: Example of microstructures.

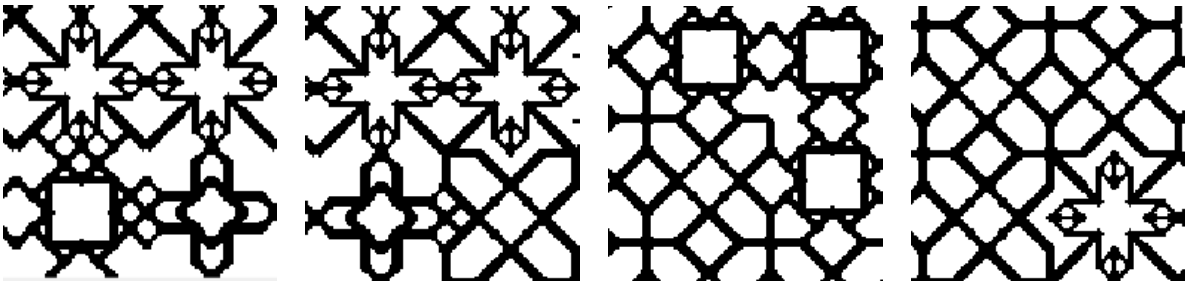

(a) Example 1 of connection to structure a.

(b) Example 2 of connection to structure a.

(c) Example 1 of connection to structure b.

(d) Example 2 of connection to structure b.

Figure 9: Example of microstructure connection.

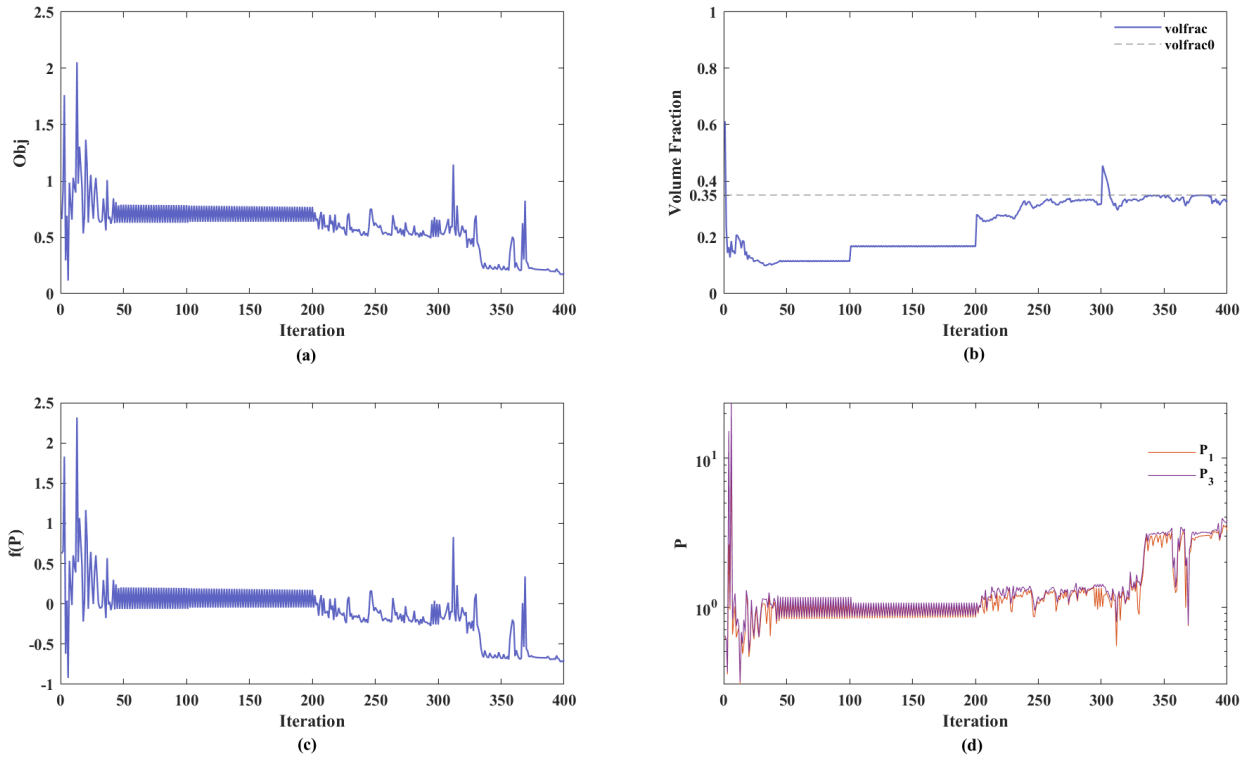

Figure 10: Iteration history of a typical lattice in Fig. 8(e): (a) Objective function; (b) Volume fraction; (c) $f(P)$ in Eq. (22); (d) eigenvalues P_1, P_3.

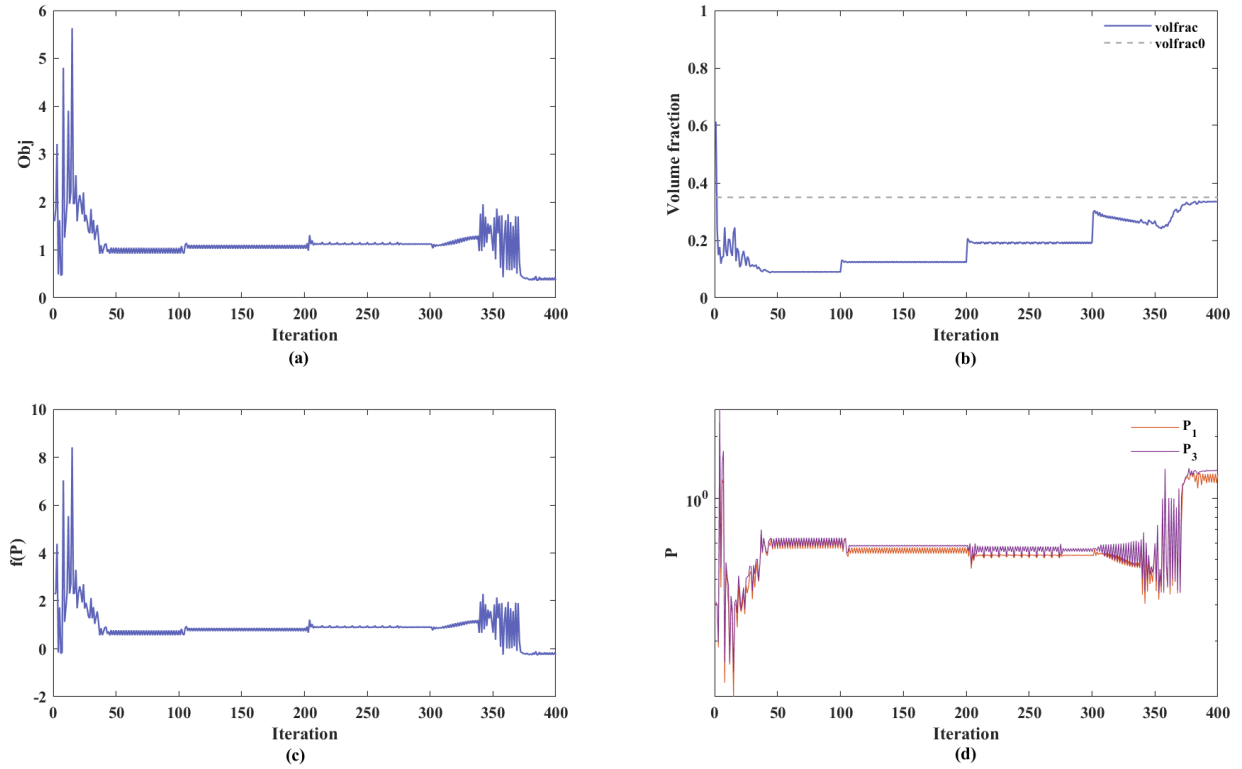

Figure 11: Iteration history of a typical lattice in Fig. 7(d): (a) Objective function; (b) Volume fraction; (c) $f(P)$ in Eq. (22); (d) eigenvalues P_1, P_3.

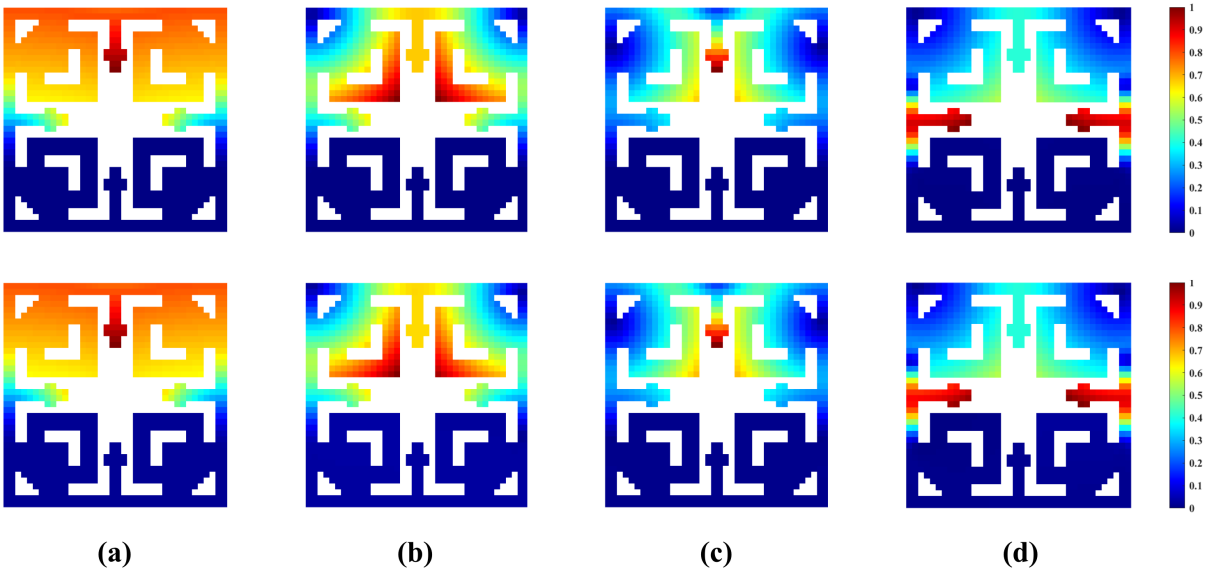

Figure 12: Comparison of eigenmodes obtained from ANASYS (top) and from ours (bottom) at eigenvalues (a) 24182, (b) 31691, (c) 64052 and (d) 119340. The Cosine similarity in Eq. (37) is respectively of 0.9997, 0.9981, 0.9996, 0.9994.

are.

The 1st, 2nd, 3rd and 4th buckling modes from a typical microstructure were compared in Fig. 12 with those derived from ANASYS. The similarity measure is respectively 0.9997, 0.9981, 0.9996, 0.9994, demonstrating nearly identical values. Their associated eigenvalues are 24182, 31691, 64052 and 119340.

6.3. Self-supporting bridge design problem

In order to test the approach's ability in designing different types of microstructures, the above bridge design problem was additionally tested in designing self-supporting microstructures so that the resulted structure naturally satisfies the self-supporting requirements in additive manufacturing. We prescribe the condition by requiring its hanging angle is not less than $\pi/4$. The basic model consisting of self-supporting lattices shown in Fig. 13 was taken, where each rod was at 45 degrees to the printing direction, ensuring the final obtained overall structure is self-supporting.

The obtained results under different weights of buckling constraint were shown in Fig. 14, where the overall structural compliance was $28.0892, 25.2472, 28.4533, 22.3849$, and 25.2772 separately. Compared with the results in Section 6.1, the introduction of the self-supporting constraint caused a significant decrease in the overall stiffness performance of the structure, although they were generally within an acceptable range and did not incur additional computational costs.

6.4. Discussions

As seen from the above typical numerical examples, the proposed approach has demonstrated its effectiveness in generating lattice structures with improved buckling strength. It fills the FMO directed macro-domain with a small number of cell-adaptive lattices, which together produce a lattice structure with optimized macro-stiffness and local buckling strength. Some related technical details are further discussed below.

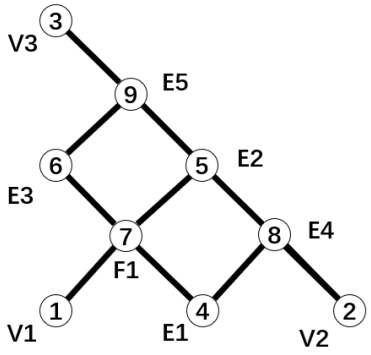

Figure 13: The basic model of the one-eighth lattice for the self-supporting microstructure using 10 rods determined by 9 points as design variables. The design variable is the thickness of each rod.

After the FMO process, different material elements are clustered into a small number typical cells. Generally, a larger cluster number is chosen a better macro-structure is generated. The cluster number can be chosen automatically based on, for example, Gap Statistics [64]. It was set 5 in our examples after testing, which provided close compliance approximation. More discussions on the clustering performance at different cluster numbers are referred to our previous work [48].

Each type of clustered elements is filled with the same lattice cell, which, together with lattices of other types, produces the macroscale lattice structure. Maintaining the connection between adjacent lattices is a very challenging topic in density-based topology optimization [65, 45, 66]. This is achieved in this study from two main aspects: using a symmetric base lattice for ease of connection, and a postprocessing to link disconnected neighboring lattices.

The base lattice is generated from anisotropic or isotropic material determined from the FMO or FIMO process in the macroscale level. In our numerical examples, the lattice cells were set with 1/8 symmetry in 2D for an overall connection and ease of implementation. The restriction on the other hand may reduce the range of the base lattices. As one of our research focus, we are also exploring approaches in designing freeform lattices while simultaneously maintaining their geometric connection.

The base lattice structure is determined by its node number, node location and their connections, and also range of the lattice beam radius. All the design DOFs together have to satisfy the cell's prescribed volume fraction, and to meet the fabrication constraints, such as self-supporting or beam-beam angle, which restrict the types of the candidate lattices. Note that radii of the optimized beams have to be above the printer's resolution as well. The geometrically specific design parameter also has its specific advantage of mesh independence in spite that different underlying FE mesh may influence the analysis accuracy.

7. Conclusion

This paper proposes and implements a multi-lattice structure optimization method that enables the selective design and filling of several different kinds of lattice structures within the model to meet the overall rigidity and local buckling requirements. It is achieved via consecutive steps of FMO to obtain the optimal material elasticity tensor distribution, and inverse homogenization to achieve a cell lattice that matches the target elasticity tensor as well as satisfies the buckling

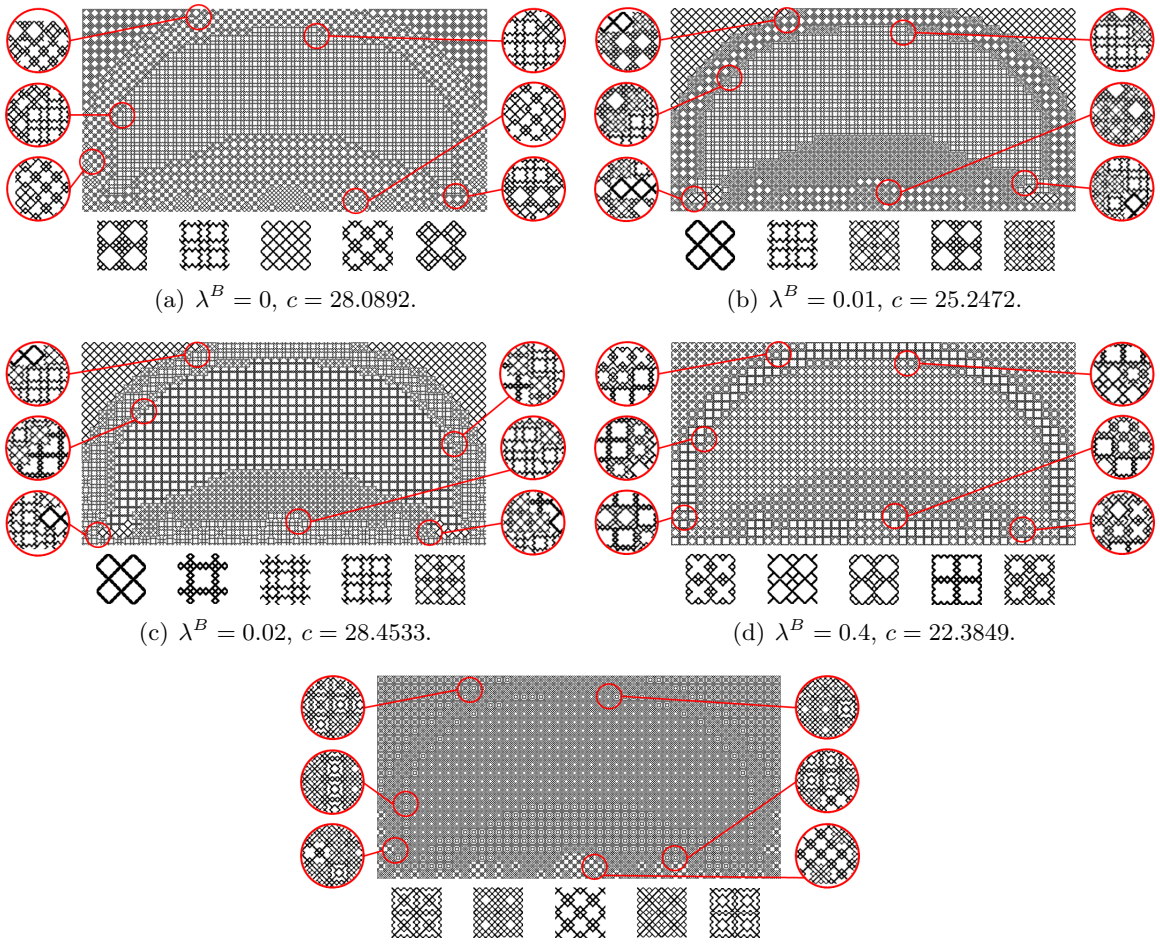

(a) $\lambda^B = 0$, $c = 28.0892$. (b) $\lambda^B = 0.01$, $c = 25.2472$.

(c) $\lambda^B = 0.02$, $c = 28.4533$. (d) $\lambda^B = 0.4$, $c = 22.3849$.

(e) $\lambda^B = 0.9$, $c = 25.2772$.

Figure 14: Results of the self-supporting bridge problem.

constraints. During the process, a machine learning approach is also devised to significantly reduce the number of material/lattice types and thus the overall computational costs.

In contrast to density-based topology optimization approaches, this approach extends the macroscale design space and imposes stronger local buckling that enhances the structural mechanical properties. It also uses the shape parameters of a fixed type of lattice structure of varied topology as design variables to ensure the geometric validity of the final lattice structure and the convergence of the optimization algorithm. The lattice within in each type of clustered cell is optimized at its location specific stress to increase its compatibility with the macro-structure's deformation. At present, an assumption of cell-periodic wavelengths of the local buckling mode is taken here. Utilizing approaches based on the Bloch-Floquet theory will further take account of the long wavelength buckling spanning several macro-cells [29, 34, 36, 37, 38], and will be explored in our future study.

Our separated FMO and lattice optimization is able to reduce the original complex nonlinear optimization problem into two simpler sub-problems, each of which may be separately optimized. The overall design DOFs and computational complexity are reduced consequently. On the other

hand, once the lattice cells are generated and embedded within the macro-structure, the macro-structure's property becomes different from that of its FMO counterpart. Repeating several time such optimization may help produce a better lattice structure. On the other hand, it is always an important issue in design optimization to balance the both critical but conflicting issues of structure validity and design choices, which is one of our current research focuses.

Acknowledgments

We would like to thank all the anonymous reviewers for their valuable comments and suggestions. The work of M. Li is partially supported by the National Key Research and Development Program of China (No. 2020YFC2201303), the NSF of China (No. 61872320), the Key R&D Program of Zhejiang Province (No. 2022C01025), the Zhejiang Provincial Science and Technology Program in China (No. 2021C01108). The work of Y. Song is supported by the Humboldt Research Fellowship for postdoctoral researchers. The work of K. Zhang is supported by the NSF of China (No. 11871245 and 12271207), and by the National Key Research and Development Program of China (No. 2020YFA0713602). We also thank Chengfeng Lin for implementing the comparison examples.

References

[1] I. Elnasri, S. Pattofatto, H. Zhao, H. Tsitsiris, F. Hild, Y. Girard, Shock enhancement of cellular structures under impact loading: Part I experiments, Journal of the Mechanics and Physics of Solids 55 (12) (2007) 2652–2671.

[2] T. A. Schaedler, C. J. Ro, A. E. Sorensen, Z. Eckel, S. S. Yang, W. B. Carter, A. J. Jacobsen, Designing metallic microlattices for energy absorber applications, Advanced Engineering Materials 16 (3) (2014) 276–283.

[3] I. S. Golovin, H.-R. Sinning, Damping in some cellular metallic materials, Journal of Alloys and Compounds 355 (1) (2003) 2–9.

[4] C. Jansari, S. P. Bordas, E. Atroshchenko, Design of metamaterial-based heat manipulators by isogeometric shape optimization, International Journal of Heat and Mass Transfer 196 (2022) 123201.

[5] E. W. Andrews, L. J. Gibson, The influence of cracks, notches and holes on the tensile strength of cellular solids, Acta Materialia 49 (15) (2001) 2975–2979.

[6] V. Krokos, S. P. A. Bordas, P. Kerfriden, A graph-based probabilistic geometric deep learning framework with online physics-based corrections to predict the criticality of defects in porous materials, ArXiv abs/2205.06562 (2022).

[7] J. Liu, A. T. Gaynor, S. Chen, Z. Kang, K. Suresh, A. Takezawa, L. Li, J. Kato, J. Tang, C. C. Wang, L. Cheng, X. Liang, A. C. To, Current and future trends in topology optimization for additive manufacturing, Structural and Multidisciplinary Optimization 57 (6) (2018) 2457–2483.

[8] Y. S. Leung, T. H. Kwok, X. Li, Y. Yang, C. C. Wang, Y. Chen, Challenges and status on design and computation for emerging additive manufacturing technologies, Journal of Computing and Information Science in Engineering 19 (2) (2019) 1–21.

[9] C. Suarez-Afanador, R. Cornaggia, N. Lahellec, A. Maurel-Pantel, D. Boussaa, H. Moulinec, S. Bordas, Effective thermo-viscoelastic behavior of short fiber reinforced thermo-rheologically simple polymers: An application to high temperature fiber reinforced additive manufacturing, European Journal of Mechanics - A/Solids 96 (2022) 104701.

[10] V. Petrovic, J. Vicente Haro Gonzalez, O. Jordá Ferrando, J. Delgado Gordillo, J. Ramón Blasco Puchades, L. Portolés Griñan, Additive layered manufacturing: sectors of industrial application shown through case studies, International Journal of Production Research 49 (4) (2011) 1061–1079.

[11] C. Mota, D. Puppi, F. Chiellini, E. Chiellini, Additive manufacturing techniques for the production of tissue engineering constructs, Journal of Tissue Engineering and Regenerative Medicine 9 (3) (2015) 174–190.

[12] G. Dong, Y. Tang, Y. F. Zhao, A survey of modeling of lattice structures fabricated by additive manufacturing, Journal of Mechanical Design 139 (10) (2017) 100906.

[13] F. Tamburrino, S. Graziosi, M. Bordegoni, The design process of additively manufactured mesoscale lattice structures: A review, Journal of Computing and Information Science in Engineering 18 (4) (2018).

[14] O. Sigmund, Materials with prescribed constitutive parameters: An inverse homogenization problem, International Journal of Solids and Structures 31 (17) (1994) 2313 – 2329.
[15] O. Sigmund, Tailoring materials with prescribed elastic properties, Mechanics of Materials 20 (4) (1995) 351–368.
[16] E. C. N. Silva, S. Nishiwaki, J. S. O. Fonseca, N. Kikuchi, Optimization methods applied to material and flextensional actuator design using the homogenization method, Computer Methods in Applied Mechanics and Engineering 172 (1-4) (1999) 241–271.
[17] J. Li, H. Liu, Optimal shape for a nozzle design problem using an arbitrary lagrangian-eulerian finite element method, J. Inverse Ill-posed Probl. 22 (1) (2014) 9–30.
[18] J. Lin, H. Zhang, Mathematical theory for topological photonic materials in one dimension, SIAM Journal on Scientific Computing (2021).
[19] H. Wang, Y. Chen, D. W. Rosen, A hybrid geometric modeling method for large scale conformal cellular structures, in: International Design Engineering Technical Conferences and Computers and Information in Engineering Conference, Vol. 47403, 2005, pp. 421–427.
[20] J. Wu, Continuous optimization of adaptive quadtree structures, Computer-Aided Design 102 (2018) 72–82.
[21] J. Wu, W. Wang, X. Gao, Design and optimization of conforming lattice structures, IEEE Transactions on Visualization and Computer Graphics 27 (1) (2019) 43–56.
[22] Y. Yu, H. Liu, K. Qian, H. Yang, M. McGehee, J. Gu, D. Luo, L. Yao, Y. J. Zhang, Material characterization and precise finite element analysis of fiber reinforced thermoplastic composites for 4D printing, Computer-Aided Design 122 (2020) 102817.
[23] O. Sigmund, S. Torquato, Design of materials with extreme thermal expansion using a three-phase topology optimization method, Journal of the Mechanics and Physics of Solids 45 (6) (1997) 1037–1067.
[24] L. V. Gibiansky, O. Sigmund, Multiphase composites with extremal bulk modulus, Journal of the Mechanics and Physics of Solids 48 (3) (1998) 461–498.
[25] M. Neves, H. Rodrigues, J. Guedes, Optimal design of periodic linear elastic microstructures, Computers and Structures 76 (1-3) (2000) 421–429.
[26] O. Sigmund, On the optimality of bone microstructure, in: IUTAM Symposium on Synthesis in Bio Solid Mechanics, Springer, 1999, pp. 221–234.
[27] J. Bauer, A. Schroer, R. Schwaiger, O. Kraft, Approaching theoretical strength in glassy carbon nanolattices, Nature Materials 15 (4) (2016) 438–443.
[28] M. M. Neves, H. Rodrigues, J. M. Guedes, Generalized topology design of structures with a buckling load criterion, Structural Optimization 10 (2) (1995) 71–78.
[29] M. M. Neves, O. Sigmund, M. P. Bendsoe, Topology optimization of periodic microstructures with a penalization of highly localized buckling modes, International Journal for Numerical Methods in Engineering 54 (6) (2002) 809–834.
[30] R. Kemmler, Topology optimization including geometrically nonlinear response, in: Proceedings of the 3rd World Congress of Structural and Multidisciplinary Optimization, 1999, pp. 17–21.
[31] T. Buhl, C. Pedersen, O. Sigmund, Stiffness design of geometrically nonlinear structures using topology optimization, Structural and Multidisciplinary Optimization 19 (2) (2000) 93–104.
[32] T. E. Bruns, D. A. Tortorelli, Topology optimization of non-linear elastic structures and compliant mechanisms, Computer Methods in Applied Mechanics and Engineering 190 (26-27) (2001) 3443–3459.
[33] M. P. Bendsoe, N. Triantafyllidis, Scale effects in the optimal design of a microstructured medium against buckling, International Journal of Solids and Structures 26 (7) (1990) 725–741.
[34] M. M. Neves, Analysis and continuum topology optimization of periodic solids with linearized elastic buckling criterion, in: IUTAM Symposium on Topological Design Optimization of Structures, Machines and Materials, Springer, 2006, pp. 99–106.
[35] C. R. Thomsen, F. Wang, O. Sigmund, Buckling strength topology optimization of 2D periodic materials based on linearized bifurcation analysis, Computer Methods in Applied Mechanics and Engineering 339 (2018) 115–136.
[36] F. Wang, O. Sigmund, Numerical investigation of stiffness and buckling response of simple and optimized infill structures, Structural and Multidisciplinary Optimization 61 (6) (2020) 2629–2639.
[37] F. Wang, O. Sigmund, 3D architected isotropic materials with tunable stiffness and buckling strength, Journal of the Mechanics and Physics of Solids 152 (2021) 104415.
[38] C. F. Christensen, F. Wang, O. Sigmund, Multiscale topology optimization considering local and global buckling response, ArXiv abs/2210.11477 (2022).
[39] X. Gao, Y. Li, H. Ma, G. Chen, Improving the overall performance of continuum structures: A topology optimization model considering stiffness, strength and stability, Computer Methods in Applied Mechanics and

Engineering 359 (2020) 112660.
[40] M. C. Fernandes, J. Aizenberg, J. C. Weaver, K. Bertoldi, Mechanically robust lattices inspired by deep-sea glass sponges, Nature Materials 20 (2) (2021) 237–241.
[41] N. Aage, E. Andreassen, B. S. Lazarov, O. Sigmund, Giga-voxel computational morphogenesis for structural design, Nature 550 (7674) (2017) 84–86.
[42] W. Zhang, Y. Zhou, J. Zhu, A comprehensive study of feature definitions with solids and voids for topology optimization, Computer Methods in Applied Mechanics and Engineering 325 (2017) 289–313.
[43] P. Vannucci, Anisotropic Elasticity, Springer, 2018.
[44] M. Kočvara, M. Stingl, J. Zowe, Free material optimization: recent progress, Optimization 57 (1) (2008) 79–100.
[45] J. Hu, M. Li, X. Yang, S. Gao, Cellular structure design based on free material optimization under connectivity control, Computer-Aided Design 127 (2020) 102854.
[46] F. Schury, M. Stingl, F. Wein, Efficient two-scale optimization of manufacturable graded structures, SIAM Journal on Scientific Computing 34 (6) (2012) B711–B733.
[47] J. M. Podestá, C. G. Mendez, S. Toro, A. E. Huespe, J. Oliver, Material design of elastic structures using voronoi cells, International Journal for Numerical Methods in Engineering 115 (3) (2018) 269–292.
[48] X. Yang, M. Li, Free isotropic material optimization via second order cone programming, Computer-Aided Design 115 (2019) 52–63.
[49] X. Yang, M. Li, Discrete multi-material topology optimization under total mass constraint, Computer-Aided Design 102 (2018) 182–192.
[50] T. M. Mitchell, Machine Learning, McGraw-Hill, 1997.
[51] D. Chen, M. Skouras, B. Zhu, W. Matusik, Computational discovery of extremal microstructure families, Science Advances 4 (1) (2018) 7005.
[52] L. Wang, Y. C. Chan, F. Ahmed, Z. Liu, P. Zhu, W. Chen, Deep generative modeling for mechanistic-based learning and design of metamaterial systems, Computer Methods in Applied Mechanics and Engineering 372 (2020) 113377.
[53] E. Andreassen, C. S. Andreasen, How to determine composite material properties using numerical homogenization, Computational Materials Science 83 (2014) 488–495.
[54] M. P. Bendsøe, N. Kikuchi, Generating optimal topologies in structural design using a homogenization method, Computer Methods in Applied Mechanics and Engineering 71 (2) (1988) 197 – 224.
[55] J. Zeman, J. Vondřejc, J. Novák, I. Marek, Accelerating a fft-based solver for numerical homogenization of periodic media by conjugate gradients, Journal of Computational Physics 229 (21) (2010) 8065–8071.
[56] L. Beex, O. Rokoš, J. Zeman, S. Bordas, Higher-order quasicontinuum methods for elastic and dissipative lattice models: uniaxial deformation and pure bending, GAMM-Mitteilungen 38 (2) (2015) 344–368.
[57] O. Rokoš, L. Beex, J. Zeman, R. Peerlings, A variational formulation of dissipative quasicontinuum methods, International Journal of Solids and Structures 102-103 (2016) 214–229.
[58] M. Tyburec, M. Doškář, J. Zeman, M. Kružík, Modular-topology optimization of structures and mechanisms with free material design and clustering, Computer Methods in Applied Mechanics and Engineering 395 (2022) 114977.
[59] M. Li, J. Hu, Analysis of heterogeneous structures of non-separated scales using curved bridge nodes, Computer Methods in Applied Mechanics and Engineering 392 (2022) 114582.
[60] X. Gao, L. Li, H. Ma, An adaptive continuation method for topology optimization of continuum structures considering buckling constraints, International Journal of Applied Mechanics 9 (07) (2017) 1750092.
[61] C. Zillober, A globally convergent version of the method of moving asymptotes, Structural Optimization 6 (3) (1993) 166–174.
[62] J. Löfberg, YALMIP: A toolbox for modeling and optimization in MATLAB, in: 2004 IEEE International Conference on Robotics and Automation, 2004, pp. 284–289.
[63] A. G. Weldeyesus, M. Stolpe, A primal-dual interior point method for large-scale free material optimization, Computational Optimization and Applications 61 (2) (2015) 409–435.
[64] R. Tibshirani, G. Walther, T. J. Hastie, Estimating the number of clusters in a data set via the gap statistic, Journal of the Royal Statistical Society: Series B (Statistical Methodology) 63 (2000).
[65] E. Garner, H. M. Kolken, C. C. Wang, A. A. Zadpoor, J. Wu, Compatibility in microstructural optimization for additive manufacturing, Additive Manufacturing 26 (2019) 65–75.
[66] J. Wu, O. Sigmund, J. P. Groen, Topology optimization of multi-scale structures: a review, Structural and Multidisciplinary Optimization 63 (3) (2021) 1455–1480.